On the origin of optical and IR emission lines in star forming galaxies

Mariela Martínez-Paredes[1]★, Gustavo Bruzual[2]†, Christophe Morisset[3], Minsun Kim[1], Marcio Meléndez[4] and Luc Binette[3]

[1]*Korea Astronomy and Space Science Institute 776, Daedeokdae-ro, Yuseong-gu, Daejeon, Republic of Korea (34055)*
[2]*Instituto de Radioastronomía y Astrofísica, Universidad Nacional Autónoma de México, Morelia, 58089 Michoacán, México*
[3]*Instituto de Astronomía, Universidad Nacional Autónoma de México, Apdo. Postal 70264, 04510 CdMx, México*
[4]*Space Telescope Science Institute, Baltimore, MD 21218, USA*

arXiv:2308.05604v1 [astro-ph.GA] 10 Aug 2023

Accepted 2023 August 10. Received Received 2023 August 9; in original form 2023 May 5

ABSTRACT

Combining the Cloudy photoionization code with updated stellar population synthesis results, we simultaneously model the MIR [Ne III]/[Ne II] vs. [O IV]/[Ne III], the MIR-FIR [Ne III]/[Ne II] vs. [O IV]/[O III] and the classical BPT diagnostic diagrams. We focus on the properties of optically classified H II galaxies that lie in the normal star forming zone in the MIR diagnostic diagram. We find that a small fraction of our models lie in this zone, but most of them correspond to the lowest explored metallicity, $Z_* = 0.0002$, at age $\sim$ 1 Gyr. This value of Z_* is, by far, lower than the values derived for these galaxies from optical emission lines, suggesting that the far-UV emission produced by post-AGB stars (a.k.a. HOLMES, hot low-mass evolved stars) is NOT the source of ionization. Instead, shock models can easily reproduce this part of the MIR diagram. We suggest that it is likely that some of these galaxies have been misclassified and that in them, shocks, produced by a weak AGN-outflow, could be an important source of ionizaton. Using a subset of our models, we derive a new demarcation line for the maximal contribution of retired galaxies in the BPT diagram. This demarcation line allows for a larger contamination from the neighbouring AGN-dominated region. Considering the importance of disentangling the different ionising mechanisms in weak or deeply obscured systems, new observational efforts to classify galaxies both in the optical and IR are required to better constrain this kind of models and understand their evolutionary paths.

Key words: galaxies: H II– infrared: galaxies

1 INTRODUCTION

The optical-line diagnostic diagram (BPT diagram Baldwin, Phillips & Terlevich 1981; Veilleux & Osterbrock 1987), based on the [O III] λ5007Å/Hβ and [N II] λ6583Å/Hα emission line ratios, has been a successful tool for distinguishing the thermal emission resulting from star formation from the non-thermal emission produced in the central engine of active galactic nuclei (AGNs, e.g., Kauffmann et al. 2003; Groves, Dopita, & Sutherland 2004; Kewley et al. 2006; Stasińska et al. 2006; Farrah et al. 2007; Levesque et al. 2010; Richardson et al. 2016; Zhang et al. 2020). However, the BPT diagram, based on the least extinguished optical emission lines, fails to distinguish these contributions in optically obscured systems (e.g., dusty galaxies), where starburst galaxies (SB) and AGNs coexist (e.g., Satyapal et al. 2008; Goulding & Alexander 2009; Meléndez et al. 2014). The BPT diagram has also limitations identifying retired galaxies, in which star formation stopped several Gyr ago and excitation is due to the presence of hot post Asymptotic Giant Branch (pAGB) stars, also known as HOLMES (hot low-mass evolved stars, Stasińska, Trevisan, & Vale Asari 2022; Stasińska et al. 2015; Flores-Fajardo et al. 2011; Stasińska et al. 2008). Mid-infrared (MIR) wavelengths offer a window in which the effects of extinction are minimal. The high resolution *Spitzer* spectra have been widely used to build MIR diagnostic diagrams that allow to differentiate the relative contributions from AGN and star forming (SF) regions (e.g., Genzel et al. 1998; Sturm et al. 2002; Peeters, Spoon & Tielens 2004; Sturm et al. 2006; Weedman et al. 2006; Dale et al. 2006; Brandl et al. 2006; Spoon et al. 2007; Armus et al. 2007; Hunter & Kaufman 2007; Farrah et al. 2007; Meléndez et al. 2008; Hao et al. 2009).

Weaver et al. (2010) used a hard X-ray (14-195 keV) selected sample of local ($z \sim 0.025$) type 1 and 2 Seyfert galaxies with high resolution *Spitzer* spectra, to investigate how the [Ne III] λ15.6μm/[Ne II] λ12.8μm and [O IV] λ25.9μm/[Ne III] λ15.6μm line ratios compare with the ratios measured in a sample of Blue Compact Dwarf (BCD, Hao et al. 2009), H II (also named normal-SF, Goulding & Alexander 2009) and SB (Bernard-Salas et al. 2009) galaxies. Three zones (quadrants) were identified in this MIR diagnostic diagram, listed in Table 1 and shown schematically in Fig. 1 (see Weaver et al. 2010, their figure 9).

Using the Cloudy[1] photoionization code (Ferland et al. 2017)

★ E-mail: mariellauriga@gmail.com
† E-mail: g.bruzual@irya.unam.mx

[1] https://gitlab.nublado.org/cloudy/cloudy/-/wikis/home

© 2022 The Authors

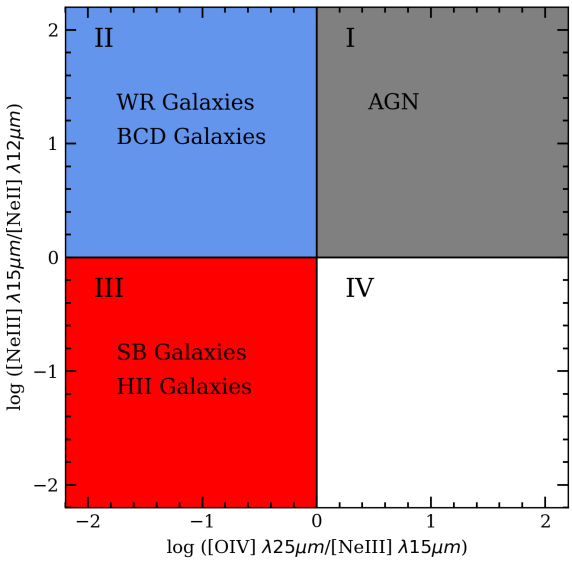

Figure 1. Schematic MIR diagnostic diagram defined by Weaver et al. (2010, their figure 9). The boundaries of the different zones are defined in Table 1. Wolf-Rayet (WR) and BCD galaxies fall preferentially in quadrant II, SB and HII galaxies in quadrant III, and AGN in quadrant I. The low ionization narrow emission regions (LINERs) extend over the AGN zone and quadrant III. ULIRGs fall mostly in quadrant III and quasars in quadrant I. Quadrant IV is mostly void of objects.

Table 1. MIR diagnostic diagram (Weaver et al. 2010).

Quadrant	$\log \frac{[\mathrm{O\,IV}]\,\lambda 25.9\mu\mathrm{m}}{[\mathrm{Ne\,III}]\,\lambda 15.6\mu\mathrm{m}}$	$\log \frac{[\mathrm{O\,IV}]\,\lambda 25.9\mu\mathrm{m}}{[\mathrm{Ne\,III}]\,\lambda 15.6\mu\mathrm{m}}$
I	$\gtrsim 0$	$\gtrsim 0$
II	$\lesssim 0$	$\gtrsim 0$
III	$\lesssim 0$	$\lesssim 0$
IV	$\gtrsim 0$	$\lesssim 0$

and the stellar libraries from Starburst99[2] (Leitherer et al. 1999), Meléndez et al. (2014) produced an extensive set of photoionization models where they successfully modelled the AGN and the BCD galaxy zones, but failed modelling the SB and H II galaxy zone. They tested a two-zone SB model to see if they could understand the normal-SF region (quadrant III). However, this resulted in a highly degenerated solution, due to the large number of stellar and physical parameters involved. Fernández-Ontiveros et al. (2016) carried out a similar approach, but in addition to the MIR [O IV] λ25.9μm/[Ne III] λ15.6μm ratio, they included the far-IR (FIR) [O IV] λ25.9μm/[O III] λ88μm emission line ratio proposed by Spinoglio et al. (2015), assuming a single zone model. As in Meléndez et al. (2014), Fernández-Ontiveros et al. (2016) were unable to model the normal-SF zone. Both groups argued that accurate modelling of the normal-SF zone requires a better treatment of the stellar atmospheres above 54.94 eV.

The [O IV] λ25.9μm line, with ionization energy[3] E_{IP} = 77.41 eV, is among the species requiring the highest ionization energy that is observable with the *Spitzer* Infra Red Spectrograph (IRS) in the spectrum of galaxies and AGNs (Genzel et al. 1998; Lutz et al. 1998). This line tracks recent star formation activity, when the intrinsic luminosity of the AGN can be up to 20 times lower than the host galaxy (Pereira-Santaella et al. 2010), and is a good indicator of AGN activity in Seyfert galaxies (Genzel et al. 1998; Meléndez et al. 2008; Pereira-Santaella et al. 2010; Weaver et al. 2010). On the other hand, the intermediate-ionization [Ne III] λ15.6μm (40.96 eV) and [O III] λ88μm (35.12 eV) lines are present in the *Spitzer* spectrum of composite systems where SB and AGN coexist, while the low-ionization [Ne II] (21.57 eV) line tracks recent star formation activity (Ho & Keto 2007). In the Weaver et al. (2010) MIR diagnostic diagram, some H II galaxies go undetected in [O IV] λ25.9μm and, when detected, there is sometimes a mixed-up optical classification, with some galaxies being classified as Seyfert or LINER.

In this Paper we use the Cloudy photoionization code (Ferland et al. 2017, c17.03) and the revised version of the Bruzual & Charlot (2003) stellar population synthesis models introduced in Plat et al. (2019, hereafter C&B models) to analyze a small sample of galaxies presenting optical and MIR emission lines, aiming at discovering: *(i)* the star forming and physical properties characterizing the galaxy population in the normal-SF zone of the MIR diagnostic diagram, *(ii)* the maximum contribution to the ionizing radiation from HOLMES allowed in this zone, and *(iii)* the position in the BPT diagram of galaxies that in the MIR diagnostic diagram lie in the normal-SF and SB zones. The paper is organized as follows. In Sec. 2 we select our sample. In Sec. 3 we describe the stellar models and the Cloudy input parameters. We present the analysis of our results for the MIR in Sec. 4 and for the optical in Sec. 5, where we define a new HOLMES demarcation line. The summary and conclusions are presented in Sec. 6.

2 MIR AND OPTICAL DATA

To compare with our photoionization model predictions, we collect from the available literature the optical ([O III] λ5007Å, [N II] λ6583Å, Hα, and Hβ) and MIR ([Ne III] λ15.6μm, [Ne II] λ12.8μm, and [O IV] λ25.9μm) emission line measurements, corresponding to the same nuclear region, for AGN, SB, and H II galaxies. Our final sample is listed in Table 2. From the *Spitzer* Infrared Nearby Galaxy Survey (SINGS, Dale et al. 2006, 2009; Moustakas et al. 2010), we select data in both spectral ranges for 14 AGN, 4 SB, and 4 H II galaxies. We add a sample of H II galaxies with available nuclear measurements of the FIR [O III] λ88μm emission line from *Herschel* / SPIRE (Fernández-Ontiveros et al. 2016).

We include MIR data for two AGNs recently observed with the Mid-Infrared Instrument (MIRI) on the *James Webb Space Telescope* (JWST, Álvarez-Márquez et al. 2022; Pereira-Santaella et al. 2022). NGC 6552 observed during commissioning (Program I.D #1039, P.I. D. Dicken) and NGC 7319, observed as part of the Early Release Observations (ERO; Program ID #2732; Pontoppidan et al. 2022). For NGC 6552, Álvarez-Márquez et al. (2022) report nuclear, circumnuclear (annulus of width $\sim$0.33 kpc), and central (aperture $\sim$0.88 kpc, 1.6 arcsec) emission. For NGC 7319, Pereira-Santaella et al. (2022) report emission from the nuclear region (denoted AGN) and

[2] https://www.stsci.edu/science/starburst99/docs/default.htm

[3] National Institute of Standards and Technology (NIST) Atomic Spectra Database.

Table 2. Observed nuclear MIR, FIR and optical emission line ratios of selected H II and SB galaxies, and AGN

Type	Name	λ15.6μm/λ12.8μm log ([NeIII]/[NeII])	λ25.9μm/λ15.6μm log ([OIV]/[NeIII])	λ25.9μm/λ88μm log ([OIV]/[OIII])	λ5007Å/λ4861Å log ([OIII]/H$_\beta$)	λ6584Å/λ6563Å log ([NII]/H$_\alpha$)
AGN[a]	NGC 1097	−1.072 ± 0.004	−0.983 ± 0.019	–	0.444 ± 0.835	0.191 ± 0.182
	NGC 1291	0.139 ± 0.172	−0.706 ± 0.037	–	0.629 ± 2.740	0.222 ± 0.460
	NGC 1566	−0.262 ± 0.034	−0.187 ± 0.086	–	0.626 ± 0.627	−0.065 ± 0.094
	NGC 2841	0.072 ± 0.115	−0.937 ± 0.022	–	0.324 ± 0.769	0.175 ± 0.448
	NGC 3031	−0.103 ± 0.027	−0.725 ± 0.037	–	0.499 ± 1.626	0.192 ± 0.460
	NGC 3621	−0.448 ± 0.026	−0.091 ± 0.050	–	1.039 ± 5.041	0.031 ± 0.129
	NGC 4450	−0.220 ± 0.157	−0.523 ± 0.100	–	0.508 ± 0.944	0.340 ± 0.438
	NGC 4579	−0.318 ± 0.021	−0.630 ± 0.010	–	0.638 ± 0.544	0.322 ± 0.236
	NGC 4594	0.064 ± 0.077	−0.863 ± 0.015	–	0.420 ± 1.183	0.320 ± 0.576
	NGC 4725	0.069 ± 0.268	−0.236 ± 0.119	–	0.975 ± 7.409	0.145 ± 0.828
	NGC 4826	−0.662 ± 0.006	−0.728 ± 0.004	–	0.013 ± 0.285	0.083 ± 0.132
	NGC 5033	−0.519 ± 0.012	−0.293 ± 0.040	–	0.628 ± 1.939	0.271 ± 0.345
	NGC 5194	−0.277 ± 0.011	−0.346 ± 0.018	–	0.863 ± 1.268	0.432 ± 0.199
	NGC 5866	−0.200 ± 0.084	−0.720 ± 0.038	–	0.499 ± 2.483	0.250 ± 0.657
SB galaxies[a]	NGC 1705	0.585 ± 0.977	−0.703 ± 0.035	–	0.240 ± 0.176	−1.127 ± 0.039
	NGC 2915	0.533 ± 0.380	−1.387 ± 0.012	–	0.488 ± 0.296	−1.308 ± 0.022
	Mrk 33	−0.123 ± 0.010	−1.701 ± 0.006	–	0.254 ± 0.027	−0.733 ± 0.004
	NGC 3773	−0.054 ± 0.034	−1.640 ± 0.043	–	0.173 ± 0.028	−0.825 ± 0.005
H II galaxies[a]	NGC 3351	−1.073 ± 0.005	−0.861 ± 0.066	–	−0.802 ± 0.047	−0.332 ± 0.038
	NGC 4254	−0.941 ± 0.007	−0.383 ± 0.040	–	−0.002 ± 0.233	−0.406 ± 0.037
	NGC 4569	−0.354 ± 0.016	−0.747 ± 0.022	–	−0.023 ± 0.115	−0.021 ± 0.058
	NGC 5713	−0.875 ± 0.003	−0.785 ± 0.037	–	−0.339 ± 0.048	−0.346 ± 0.014
H II galaxies[b]	NGC253	−1.141 ± 0.004	−0.121 ± 0.136	−0.332 ± 0.081	–	–
	NGC 1614	−0.595 ± 0.010	−0.863 ± 0.014	−1.227 ± 0.006	–	–
	NGC 2146	−0.836 ± 0.004	−0.674 ± 0.049	−1.770 ± 0.004	–	–
	M 82	−0.796 ± 0.015	−0.249 ± 0.083	−1.640 ± 0.003	–	–
	NGC 3184	−0.930 ± 0.014	−0.127 ± 0.161	−0.377 ± 0.248	–	–
	NGC 3256	−0.902 ± 0.003	−0.722 ± 0.047	−1.192 ± 0.016	–	–
	M95	−1.043 ± 0.007	0.440 ± 1.870	−0.301 ± 0.341	–	–
	NGC 4536	−0.764 ± 0.003	−0.551 ± 0.041	−1.773 ± 0.002	–	–
	M 83	−1.235 ± 0.003	−0.707 ± 0.037	−1.238 ± 0.011	–	–
	NGC 6946	−1.009 ± 0.003	0.026 ± 0.183	−0.479 ± 0.061	–	–
AGN[c]	NGC 6552 [d1]	0.059 ± 0.024	0.073 ± 0.014	–	–	–
	NGC 6552 [d2]	0.004 ± 0.021	−0.137 ± 0.011	–	–	–
	NGC 6552 [d3]	0.023 ± 0.024	0.010 ± 0.011	–	–	–
	NGC 7319 [e1]	0.321 ± 0.015	0.402 ± 0.007	–	–	–
	NGC 7319 [e2]	0.066 ± 0.009	−0.014 ± 0.008	–	–	–
	NGC 7319 [e3]	0.520 ± 0.033	0.243 ± 0.013	–	–	–

[a]From SINGS (Dale et al. 2006, 2009). [b]From *Herschell* / SPIRE (Fernández-Ontiveros et al. 2016). [c]From *JWST*/MIRI: [d1]Nuclear, [d2]Circumnuclear, [d3]Central (Álvarez-Márquez et al. 2022); [e1]AGN, [e2]N2, [e3]S2 (Pereira-Santaella et al. 2022).

Table 3. C&B model parameters

IMF	α	Mass range [M$_\odot$]	M$_l$ [M$_\odot$]	M$_u$ [M$_\odot$]	Z_* log (Z_*)
Kroupa (2001)	+2.30	$0.5 \leq m \leq$ M$_u$	0.1	100, 300	0.0002, 0.002, 0.008, 0.014, 0.017, 0.03, 0.06
	+1.30	M$_l \leq m < 0.5$			-3.7, -2.7. -2.1, -1.85, -1.77, -1.52, -1.22
Top-heavy (x030)	+1.30	M$_l \leq m \leq$ M$_u$	0.1	100, 300	”

Note.- Column 1 lists the IMF, defined as $\Phi(m) = dN/dm = Cm^{-\alpha} = Cm^{-(1+x)}$, where C is a normalization constant. Columns 2 to 5 give the IMF slope, mass range, and lower and upper mass limits, respectively. For the Salpeter (1955) IMF, $\alpha = 2.35$. Column 5 lists the stellar metallicities used in the C&B models.

Table 4. Physical parameters used in the photoionization models

Parameter.	Values explored	Description
SED type	'SSP', 'CSF'	Single Stellar Population and Constant Star Formation
log age [yr]	6, 6.18, 6.3, 6.4, 6.48, 6.54, 6.6, 6.65, 6.7, 6.74, 6.78, 6.81,	in SSP case
	6.85, 6.88, 6.9, 6.93, 6.95, 7, 7.48, 8, 8.18, 8.3, 8.4, 8.48, 8.54,	...
	8.6, 8.65, 8.7, 8.74, 8.78, 8.81, 8.85, 8.88, 8.9, 8.93, 8.95, 8.98,	...
	9, 9.48, 9.7 and 10.	
log age [yr]	6, 6.18, 6.3, 6.4, 6.48, 6.54, 6.6, 6.65, 6.7, 6.74, 6.78, 6.81,	in CSF case
	6.85, 6.88, 6.9, 6.95, 7, 7.48, 8, 8.48, 9, 9.48, 9.7 and 10.	...
log (U)	-1.5, -2, -2.5, -3, -3.5, -4	ionization parameter
log (n_H) [cm^{-3}]	1, 2, 3, 4	Hydrogen density
log $(O/H)_{total}$	-5.06, -4.06, -3.45, -3.20, -3.12, -2.86, -2.58	total Oxygen abundance
C/O	-1, -0.36, 0.15	
ΔN/O	-0.25, 0, 0.25	deviation from N/O to O/H ratio (Gutkin, Charlot, & Bruzual 2016)
ξ	0.36	dust-to-metal mass ratio
fr	1.0	form factor

two asymmetric radio hotspots: N2 and S2, located at 0.43 and 1.5 kpc from the nucleus, respectively.

Additionally, we select 404 AGN with clear detection of nuclear emission in the four optical emission lines from the Burst Alert Telescope on *Swift* (BAT, Koss et al. 2017). ~ 17 per cent of this sample also shows nuclear emission in the four MIR emission lines (Weaver et al. 2010).

Likewise, we select a sample of 767,738 optical emission line galaxies from SDSS DR8 (Brinchmann et al. 2004; Tremonti et al. 2004), observed with signal-to-noise ratio > 3σ, and 80 SF galaxies[4] with available [Ne III] λ15.6μm/[Ne II] λ12.8μm emission line ratio, but undetected [O IV] λ25.9μm emission (LaMassa et al. 2012). For conciseness, these objects are not listed in Table 2.

3 MODELS

3.1 Stellar populations

The stellar ingredients used in the C&B models are explained in detail in Sánchez et al. (2022, appendix A, tables 8 to 12). The C&B models include advances in the stellar evolution theory from the last decade. The models cover in detail the evolution of O and B stars, including the Wolf-Rayet (WR) phase, and treat HOLMES (pAGB stars) following Miller Bertolami (2016). Each C&B model contains 220 spectra covering the age range from 0 to 14 Gyr. In a simple stellar population (SSP) the most massive (O, B and Wolf-Rayet) stars last a few Myr, depending on their mass. During this time, the strong UV continuum emitted by these young hot stars is responsible for the ionization and excitation of the surrounding medium. At age between 70 and 500 Myr, depending on metallicity, HOLMES appear and become responsible for the far-UV emission, being the only source of photoionization (Stasińska et al. 2008). The SSP models were scaled to a typical cluster mas of 1×10^6 M$_\odot$. Besides the instantaneous burst models (SSPs), we explore models with a continuous star formation rate (SFR) at a constant value of 1 M$_\odot yr^{-1}$ (hereafter CSF models).

To test different stellar mass distributions, we use models computed from assuming a Kroupa (2001) and a Top-heavy initial mass function (IMF), with parameters listed in Table 3. Hereafter, the Top-heavy model will be denoted as x030 model to reflect its IMF slope. For both IMFs we tested models with upper mass limit of star formation, M_u = 100 and 300 M$_\odot$. In all cases, the lower mass limit is M_l = 0.1 M$_\odot$. To explore a large set of spectral energy distributions (SEDs), we select C&B models for the seven values of metallicities Z_* listed in Table 3.

In Figs. 2 and 3 we show the ionization properties of the C&B models. In SSP models, depending on the IMF, the rate of production of ionising photons in the HOLMES era is up to eight orders of magnitude lower than at early ages when the hot main sequence (MS) stars are the dominant source. The transition between these two regimes happens a few hundred Myr later in the lower Z_* than in the higher Z_* models (cf. panels *(a)* and *(b)* of Fig. 3). The photon production rates Q(H I) and Q(He I) vary weakly with Z_* as compared with its variation with the upper mass cut-off M_u. These rates span roughly one order of magnitude from young to older ages in the CSF models explored in this paper. Even though HOLMES provide 100% of the ionising photons after a few hundred Myr in SSP models, their contribution is negligible in CSF models, in which, the MS and WR stars are always the dominant sources (panel *(c)* of Fig. 3). Depending on Z_*, the contribution of WR stars to the ionising photon budget can reach up to 25%.

3.2 Shock models

A fraction of the nuclear gas in HII region galaxies may be ionized by both high velocity shocks in the ISM and supernova remnants. It is thus important to understand the contribution of shocks to their emission spectra since the size, luminosity and morphology of the nuclear HII region are sensitive to the ionizing source (see, e.g., Moumen et al. 2019; Rhea et al. 2023, and references therein).

Using MAPPINGS V[5] (Sutherland & Dopita 2017), Alarie & Morisset (2019) recalculated the models published by Allen et al. (2008), extending their calculations to lower metallicities by assuming abundances from Gutkin, Charlot, & Bruzual (2016). Their calculations include only fast (200-1000 km s^{-1}) shock models, in which the UV and soft X-ray ionizing photons are produced by hot gas cooling

[4] These galaxies are part of the *Spitzer*-SDSS-*GALEX* spectroscopy Survey and the *Spitzer* SDSS Spectroscopy Survey (SSGSS, S5; PI: D. Schiminovich).

[5] https://mappings.anu.edu.au/code/

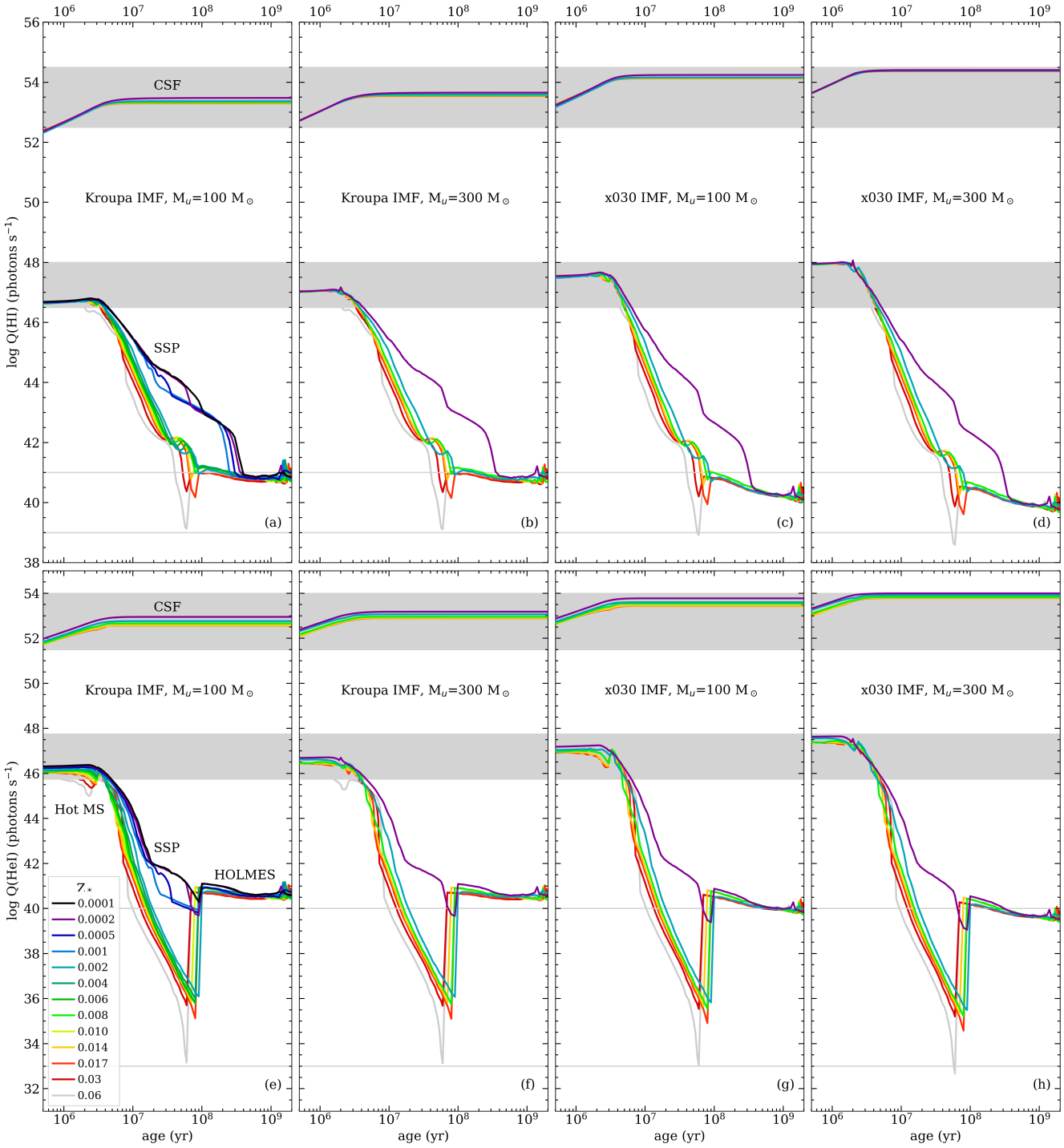

Figure 2. Production rate of H I (*top panels*) and He I (*bottom panels*) ionizing photons in the C&B stellar population models used in this work (see Table 3): *(a,e)* Kroupa IMF, $M_u = 100\,M_\odot$, *(b,f)* Kroupa IMF, $M_u = 300\,M_\odot$, *(c,g)* x030 IMF, $M_u = 100\,M_\odot$, and *(d,h)* x030 IMF, $M_u = 300\,M_\odot$. Models are colour coded according to Z_* as indicated in the legend in panel *(e)* legend. In each panel, the lower set of lines corresponds to the SSP models and the upper set to the CSF models. For the SSP models in panels *(a,e)* we indicate the age range at which the hot MS stars and the HOLMES are responsible for the ionizing radiation. The *grey horizontal lines and bands* are drawn to guide the eye when comparing the different models. For the SSP models, Q corresponds to a stellar population of mass = 1 $M_\odot$. For the CSF models the mass of the population increases continuously at a rate of 1 $M_\odot$ yr^{-1}. For illustration purposes, in panels (*a,e*) we include 6 extra SSP and CSF models, not listed in Table 3, corresponding to $Z_* = 0.0001$, 0.0005, 0.001, 0.004, 0.006, 0.01.

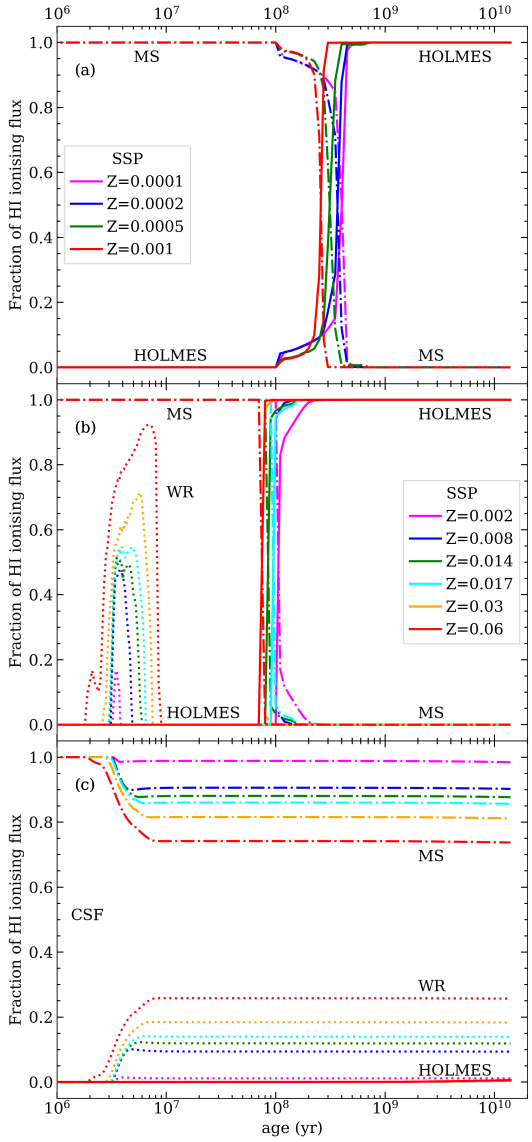

Figure 3. Fraction of H I ionising flux emitted by MS, WR and HOLMES stars vs. age (*dot-dashed, dotted* and *solid* lines, respectively. Panel *(a)* shows the 4 lowest Z_* C&B SSP models. At these metallicities, HOLMES appear at age from 200 to 500 Myr and no WR stars are expected in the stellar population. Only the $Z_* = 0.0002$ model is used in this investigation. Panel *(b)* corresponds to the other 6 Z_* SSP models in Table 3. For these metallicities the appearance of HOLMES occurs at about 70 to 100 Myr, and the contribution from WR stars is clearly seen at age ranging from 3 to 8 Myr, depending on Z_*. The transition from the MS to the HOLMES dominated regimes is clearly seen in panels *(a,b)*. Panel *(c)* shows the contribution of these stellar groups to the H I ionizing flux of the CSF models for the same Z_* values of panel *(b)*. In the CSF models the contribution of WR stars can reach 25%, whereas the contribution from HOLMES is negligible at all ages. Models in panel *(c)* are colour coded according to Z_* as indicated in the legend in panel *(b)*. In all panels we show models that assume the Kroupa IMF with $M_u = 100\,M_\odot$.

behind the shock front. Alarie & Morisset (2019) explored a larger volume of parameter space, resulting in a larger number of models than those computed by Allen et al. (2008).

3.3 Photoionization models

We use the Cloudy photoinisation code (Ferland et al. 2017, c17.03) to model the emission from gas heated by the massive young (O, B, and Wolf-Rayet) stars and HOLMES (pAGB) present in the C&B SSP and CSF models described above. We select SEDs ranging in age from 1 Myr to 10 Gyr, totalling 41 SEDs in the case of the SSP and 24 for the CSF models. In Table 4 we list the physical parameters used in our photoionization models.

To explore similar physical parameters to the ones used in previous works for SF galaxies (e.g, Dale et al. 2006; Kewley et al. 2001; Fernández-Ontiveros et al. 2016; Gutkin, Charlot, & Bruzual 2016, and references therein), we vary the hydrogen density n_H from 10^1 to 10^4 cm^{-3} in steps of powers of 10.

We choose to explore regions with a form factor $f_S = 1$ (Stasińska et al. 2015). This value means that the inner radius of the model corresponds to the value one would have obtained for the Strömgren radius, if the region would had been a filled sphere of photoionized gas. This leads to a morphology that is between the plane parallel and the filled sphere cases. The relation between the form factor f_S, the ionising photons emitted by the central source $Q(H)$, the hydrogen density $n(H)$ and the ionization parameter[6] U is taken from Stasińska et al. (2015).

The total metal content is chosen to match the stellar metallicity. The abundance of the solar nebula is adopted from Bressan et al. (2012), as in Gutkin, Charlot, & Bruzual (2016)[7]. We allow C/O and N/O to vary (see Table 4). Once the values for the total abundance ratios of O/H, N/O and C/O are defined, we obtain the gas abundance by applying a depletion to every element, using the recipes given by Gutkin, Charlot, & Bruzual (2016), with a dust-to-metal mass ratio parameter $\xi_d = 0.36$.

We include dust grains using the "ism" default dust composition in Cloudy. The amount of dust in the Cloudy models is determined by scaling the solar value by $\xi_d/0.36 \times Z/0.015$, where Z is the total metallicity.

Finally, we take several cuts in the spatial integration of the column density in the models. All Cloudy photoionization models are obtained using a stopping criteria of $H^+/H = 0.02$. No electron temperature stopping criteria is used, to avoid metal-rich models to artificially stop before reaching the recombination front. This leads to radiation-bounded (RB) models at all metallicities. From each individual model, we generate 4 other models by considering the values of the output variables (line intensities, mean values of physical parameters, ionic fractions, etc.) obtained after cutting the initial model at radii corresponding to Hβ = 80, 60, 40, and 20% of the total RB-case Hβ value.

In total, we generated 2,358,330 models, resulting from exploring two SF laws, two IMFs, two upper mass cut-offs, seven stellar and nebular metallicities, 24 ages for the SSP, 41 ages for the CSF case,

[6] The ionization parameter U is defined as:

$$U \equiv \frac{Q(H)}{4\pi r_o^2 n(H) c}, \quad (1)$$

the dimensionless ratio between the Hydrogen-ionizing photon and the total-Hydrogen densities. In Eq. (1) r_o is the distance between the ionizing source (the stellar population) and the illuminated face of the cloud (in cm), $n(H)$ is the total (ionized, neutral, and molecular) Hydrogen density in cm^{-3}, c is the speed of light, $Q(H)$ is the number of Hydrogen ionizing photons emitted by the source in s^{-1}.

[7] The initial metallicity of the solar nebula corresponds to $Z = 0.017$, and the current surface abundance of the sun to $Z = 0.015$ (Gutkin, Charlot, & Bruzual 2016, and references therein)

four electron densities, six ionization parameters, three C/O ratios, three ΔN/O departure from canonical N/O value, and six values for the cut in radius (see above).

We note that there is a large number of RB models in the normal-SF zone. These models can be associated with optically thick clouds, in which the emission of [Ne II] $\lambda 12.8 \mu$m is efficient (Meléndez et al. 2014). For each model we compute the principal optical and IR emission lines typically used to classify galaxies.

The models presented in this section are available[8] in the Mexican Million Model database (3MdB Morisset et al. 2015) [9] under the reference code CB_19. The matter-bounded (MB) models can be identified by their HbFrac parameter value.

4 IR EMISSION LINE RATIOS

Since dust extinction decreases with wavelength, IR emission lines are especially suited to explore heavily obscured galaxy nuclear regions, where copious star formation and accretion onto supermassive black holes takes place. The emission from the gas excited by hot stars provides information about both the stellar population and the surrounding gas. In this section we use the results of Sec. 3 to explore the IR emission line ratios used frequently in the literature to classify low-luminosity galaxies and/or deeply obscured systems that go undetected in the visible range.

In Fig. 4 we plot the resulting MIR diagnostic diagram for the SSP and CSF Kroupa IMF models for both $m_u = 100$ and 300 $M_\odot$. Models reaching the MB condition are shown in the *top panels*. The *bottom panels* show the RB models. MB and RB models simulate partially and totally ionized clouds, respectively. Models are colour-coded according to their metallicity. Fig. 5 shows a similar plot but for the x030 IMF models. There are no significant differences between equivalent panels in Figs. 4 and 5, implying that neither MB nor RB model predictions are sensitive to the IMF slope or the upper mass cut-off. This behaviour is expected since the parameters that affect most the SEDs are the age and the metallicity (cf. Fig. 2). Since the IMF slope and the upper mass cut-off do not affect significantly the ionizing SED, the properties of the ionized gas do not depend on these parameters.

The same behaviour is observed in the optical spectral range, see Figs. A1 and A2 in Appendix A. In the same token, Gutkin, Charlot, & Bruzual (2016) successfully modelled observations of star forming galaxies in several optical diagnostic diagrams, using a similar grid of stellar population models and gas cloud parameters. They also find marginal differences between the line emission ratios expected from models with different IMFs and upper mass limits (see their figure 6), as we do for the IR lines.

In Fig. 6 we explore the dependence of our models on U. We plot the MIR diagnostic diagram for three values of U, spanning the full range used in this investigation. A fraction of the $\log(U) = -1.5$ (left panel) models has $\log([\mathrm{O\,IV}]/[\mathrm{Ne\,III}]) > 0$, while most $\log(U) = -3$ (middle panel) and all $\log(U) = -4$ (right panel) models have $\log([\mathrm{O\,IV}]/[\mathrm{Ne\,III}]) < 0$. It is important to note that the range of values of the [O IV]/[Ne III] ratio allowed by the models is considerable larger than observed, as highlighted by the inner square in each panel of Figs. 4 - 6. The low $\log([\mathrm{O\,IV}]/[\mathrm{Ne\,III}])$ values, reaching -6, imply that there is no [O IV] emission in the cloud.

For $\log(U) < -3$ there is virtually no O^{+3} emission because the radius-averaged ionization fraction decreases, making the gas inefficient in producing [O IV] (Meléndez et al. 2014, figure 13). Despite these extremely low values of [O IV]/[Ne III] the values of [Ne III]/[Ne II] are still relevant in a Ne dominated gas, and can still be used as a single-ratio diagnostic in the absence of [O IV] emission in SF galaxies.

The SSP models allow for a wider range of values of the [O IV]/[Ne III] and [Ne III]/[Ne II] line ratios and offer a larger baseline to understand the complex nature of SF regions in galaxies, in which low and highly ionized atomic species coexist. From here on and for clarity, we will discuss only the results for the RB, $M_u = 100\,M_\odot$ Kroupa IMF SSP models, labelled (RB-SSP-Kroup-MU100) in the plots. Similar conclusions will be reached using the other sets of SSPs, including the MB models. Gutkin, Charlot, & Bruzual (2016) assumed (for simplicity) that galaxies are ionization-bounded and therefore used only RB models (labelled ionization-bounded models in their paper).

To explore how model predictions overlap with the observations, in Figs. 7 and 8 we compare our results with the sample discussed in Sec. 2 (Table 2). The cubic relation

$$\begin{aligned} \log([\mathrm{Ne\,III}]/[\mathrm{Ne\,II}]) &= 5.6 \times \log([\mathrm{O\,IV}]/[\mathrm{Ne\,III}]) \\ &+ 4.6 \times \log([\mathrm{O\,IV}]/[\mathrm{Ne\,III}])^2 \\ &+ 1.3 \times \log([\mathrm{O\,IV}]/[\mathrm{Ne\,III}])^3 + 1.5, \\ \text{for} \quad &-2 \lesssim \log([\mathrm{O\,IV}]/[\mathrm{Ne\,III}]) \lesssim -0.05, \end{aligned} \tag{2}$$

(*red solid* line in top panel of Fig. 7 and 8) represents the lower boundary of a region that encloses models of age from 100 to 1000 Myr, falling in quadrants II and III of Fig. 1. The fit in Eq. (2) excludes the extreme models with $\log([\mathrm{O\,IV}]/[\mathrm{Ne\,III}]) \gtrsim 0$, with parameters $\log(U) = -2$ and $10 \leq n_H \lesssim 10^3$ cm^{-3}. For comparison, models with $\log([\mathrm{O\,IV}]/[\mathrm{Ne\,III}]) \sim 0$ have $\log(U) = -3$ for all values of n_H.

The top panels of Fig. 6, show that only the lower metallicity models fill quadrants II and III in the range of interest shown in Fig. 1, whereas models of higher metallicity fall in quadrant III of the diagram but outside this range. The latter being dominated by stellar populations younger than 1 Gyr, with older populations having the lower metallicities (bottom panels of Fig. 6). By excluding the lowest metallicity models ($\log Z < -3$), we derive a second star forming boundary, described by the following cubic relation

$$\begin{aligned} \log([\mathrm{Ne\,III}]/[\mathrm{Ne\,II}]) &= 0.1 \times \log([\mathrm{O\,IV}]/[\mathrm{Ne\,III}]) \\ &- 0.9 \times \log([\mathrm{O\,IV}]/[\mathrm{Ne\,III}])^2 \\ &- 0.2 \times \log([\mathrm{O\,IV}]/[\mathrm{Ne\,III}])^3 + 1.1, \\ \text{for} \quad &-2 \lesssim \log([\mathrm{O\,IV}]/[\mathrm{Ne\,III}]) \lesssim -0.05, \end{aligned} \tag{3}$$

and shown as a *red dashed* line in the bottom panel of Fig, 8. Interestingly, SINGS AGNs are below this boundary.

Shocks are an important source of ionization in objects in quadrant III of the MIR diagnostic diagram. Shocks can be produced by either cloud-cloud collisions, the expansion of HII regions into the surrounding interstellar medium, outflows from young stellar objects, supernova blast waves, outflows from AGNs and starbursts, and/or galaxy collisions.

We observe a considerable increase in the number of shocks models calculated by Alarie & Morisset (2019) lying in quadrant III. Excluding models with the lowest metallicity, we derive the lower-limit for excitation produced by shocks, indicated by the *blue solid line* in Figs. 7 and 8. In Fig. 9 we plot results for shock+precursor models, which take into account the gas entering the shock front.

We highlight that it is possible that a fraction of the observed MIR emission lines in H II galaxies is due to collisional excitation

[8] https://sites.google.com/site/mexicanmillionmodels/the-different-projects/cb_19?pli=1
[9] https://sites.google.com/site/mexicanmillionmodels/

by shocks (e.g., Groves, Dopita, & Sutherland 2004). It is likely that in some HII galaxies shocks driven by a weak AGN-outflow are an important source of excitation (e.g., Cazzoli et al. 2022). For the three galaxies (NGC 253, NGC 6946, and M 95) below the lower boundaries for excitation from our photoionization (*red-solid* and *red-dashed* lines) and shock (*blue-solid* line) models in Figs. 7 and 8, it is likely that another ionising source, like a weak AGN, needs to be considered.

Feltre et al. (2023) find that in Seyfert galaxies in which the contribution from the AGN is below 50%, MIR line ratios are better modelled when shocks are added as an additional source of ionization . Recent studies have shown that the star formation activity in galaxies is highly concentrated towards their centre (Martínez-Paredes et al. 2019). Additionally, there is growing evidence indicating that the AGN dusty torus is a structure that includes a polar wind, that originates in the inner part of the torus and that is co-spatial with the outflow (e.g., Martínez-Paredes et al. 2020; García-Bernete et al. 2022, and references therein). Thus, we cannot neglect the possibility that shocks produced by stellar feedback are also an important source of ionization, especially in objects that lie close to the star forming boundary.

In general, the star forming activity of galaxies in quadrant III must occur under very special conditions, in which shocks and AGNs influence their evolution. A deeper study to disentangle their different contributions on scales of a few parsec can be carried out with *JWST*/MIRI, which offers the needed combination of high spatial resolution and sensitivity.

4.1 Discussion

Most of our models in quadrant III with the higher ratios of [O IV] λ25.9μm/[Ne III] λ15.6μm have low metallicity. However, HII galaxies in our sample have nuclear or central metallicities not far from solar abundance, with (O/H) around -3.5 to -3 (Moustakas et al. 2010; Beck et al. 2022; Kaplan et al. 2016). These metallicities have been derived from optical spectra using different methods, for example, strong-line and radial gradients (Moustakas et al. 2010). Beck et al. (2022) used the MIR spectrum and the equations from Nicholls et al. (2017).

Due to the presence of different sites of star formation within the central region of these galaxies, it is likely that some of them have a complex distribution of metallicity (e.g., Calzetti et al. 2021; Boselli et al. 2006; Barth & Shields 2000). In particular, NGC 3351 has both a circumnuclear starburst ring and a nuclear red stellar population within the first kiloparsec (Calzetti et al. 2021). For NGC 253, metallicities ranging from $\sim 0.5\,Z_{\odot}$ (Ptak et al. 1997, from the X-ray spectrum) to $\lesssim 1.5\,Z_{\odot}$ (Webster & Smith 1983, from the optical spectrum), have been reported.

In NGC 4569, a prototypical anaemic galaxy located close to the center of the Virgo Cluster, the observed nuclear optical spectrum is better modelled under a ram pressure stripping scenario. NGC 253 and NGC 4536 show some evidence of a weak AGN (e.g., Hughes et al. 2005; Mohan, Anantharamaiah, & Goss 2002). In this case, [O IV] λ25.9μm turns out to be a good indicator of AGN activity, since the emission of this line increases in presence of an AGN radiation field (e.g., Meléndez et al. 2008).

Among the H II galaxies in this sample, NGC 3351 and M95 have been identified as hot-spot galaxies, in which the central source, a LINER or a Seyfert nucleus, is surrounded by an HII region within the first kiloparsec (Sérsic 1973; Kennicutt, Keel, & Blaha 1989). Curiously, the active galaxy NGC 1097, also identified as a hot-spot galaxy, has similar MIR emission line ratios to NGC 3351, while M95 presents the highest log ([O IV] λ25.9μm/[Ne III] λ15.6μm) line ratio. On the other hand, NGC 4569 has been classified as a transition object (LINER/HII, Keel 1996; Ho, Filippenko, & Sargent 1997), in which the UV and optical properties are attributed to the presence of a young in combination with an old stellar population or AGN. However, based on the position of this galaxy in the MIR and optical BPT diagrams, the dominant ionising source thought to be HOLMES+AGN might be important in sources like NGC 5713, where many nuclear HII regions have been detected, and NGC 4254, where the spiral structure is very complex and chaotic (Eskridge et al. 2002; Martini et al. 2003; Brookes et al. 2006).

In Figs. 7 and 8 we include the nuclear and extended emission from the nearby AGNs NGC 6552 (crimson dots) and NGC 7319 (navy dots), recently observed with the *JWST*/MIRI instrument. Both objects have been identified as obscured-AGNs, with $\log N_H = 24.05$ and 23.8 [cm^{-2}], respectively. NGC 6552 has been optically classified as Seyfert 2 (Álvarez-Márquez et al. 2022, and references therein). NGC 7319 is a type 2 AGN which lacks a nuclear starburst (Pereira-Santaella et al. 2022, and references therein). Additionally, it has two asymmetric radio lobes and a compact core, likely associated with the presence of a radio jet. It shows an outflow that is co-spatial with the radio lobes, suggesting that the outflow is driven by the radio jet (e.g, Aoki et al. 1999).

For NGC 6552, we plot the emission of the nuclear (within ~ 0.58 kpc, small crimson dot), circumnuclear (between ~ 0.55 and ~ 0.88 kpc, medium crimson dot), and central (large crimson dot) regions. The nuclear and central emissions lie in the AGN zone while the circumnuclear emission shifts towards the star forming zone. Álvarez-Márquez et al. (2022) point out that the central spectrum includes the emission of the nuclear and circumnuclear regions, but it is not the sum of both of them. In the case of NGC 7319, we plot the emission from the nuclear AGN (small navy dot), from the radio hotspot N2 (medium navy dot), and from the radio hotspot S2 (large navy dot). The nuclear and S2 (located at 1.5 kpc from the unresolved radio source) emissions clearly lie in the AGN zone. However, N2 (located at 430 pc from the unresolved radio source) shifts towards the transition zone. Pereira-Santaella et al. (2022) argue that this asymmetry can be explained by the interaction of the northern radio jet (where the N2 hotspot is located) with the ISM. These results illustrate the power of the MIR diagram to classify the different excitation mechanisms present in the nuclear and circumnuclear regions of galaxies.

In Fig. 10 we plot the [Ne III]/[Ne II] vs. [O IV]/[O III] MIR-FIR diagram proposed by Fernández-Ontiveros et al. (2016) as a diagnostic diagram for SB and AGN activity. Our photoionization models reproduce about half of their sample, most likely as a result of the larger number of stellar parameters explored by us (e.g., metallicity, IMF, and age). We note that in this diagram, NGC 4536, NGC 253 and M95 lie outside of the zone covered by our photoionization models. Comparing the physical conditions in different H II regions, Kennicutt, Keel, & Blaha (1989) concluded that in H II galaxies with peculiar properties (e.g., broader and extended [O III] λ5007Å emission) like NGC 3351, a fraction of the observed line emission could be attributed to shocks or to an unresolved LINER or Seyfert nucleus surrounding an SF region. Incidentally, Ho, Filippenko, & Sargent (1997) found that in early-type spiral galaxies, like many H II galaxies, mass loss from evolved stars in the central ~ 5 pc can provide most of the fuel required by the AGN. Recent studies have found that nuclear SB can survive the strong radiation field of the AGN down to scales of a few parsec in the case of Seyfert galaxies (Esquej et al. 2014) and of a few hundred parsecs in the case of quasars (Martínez-Paredes et al. 2019).

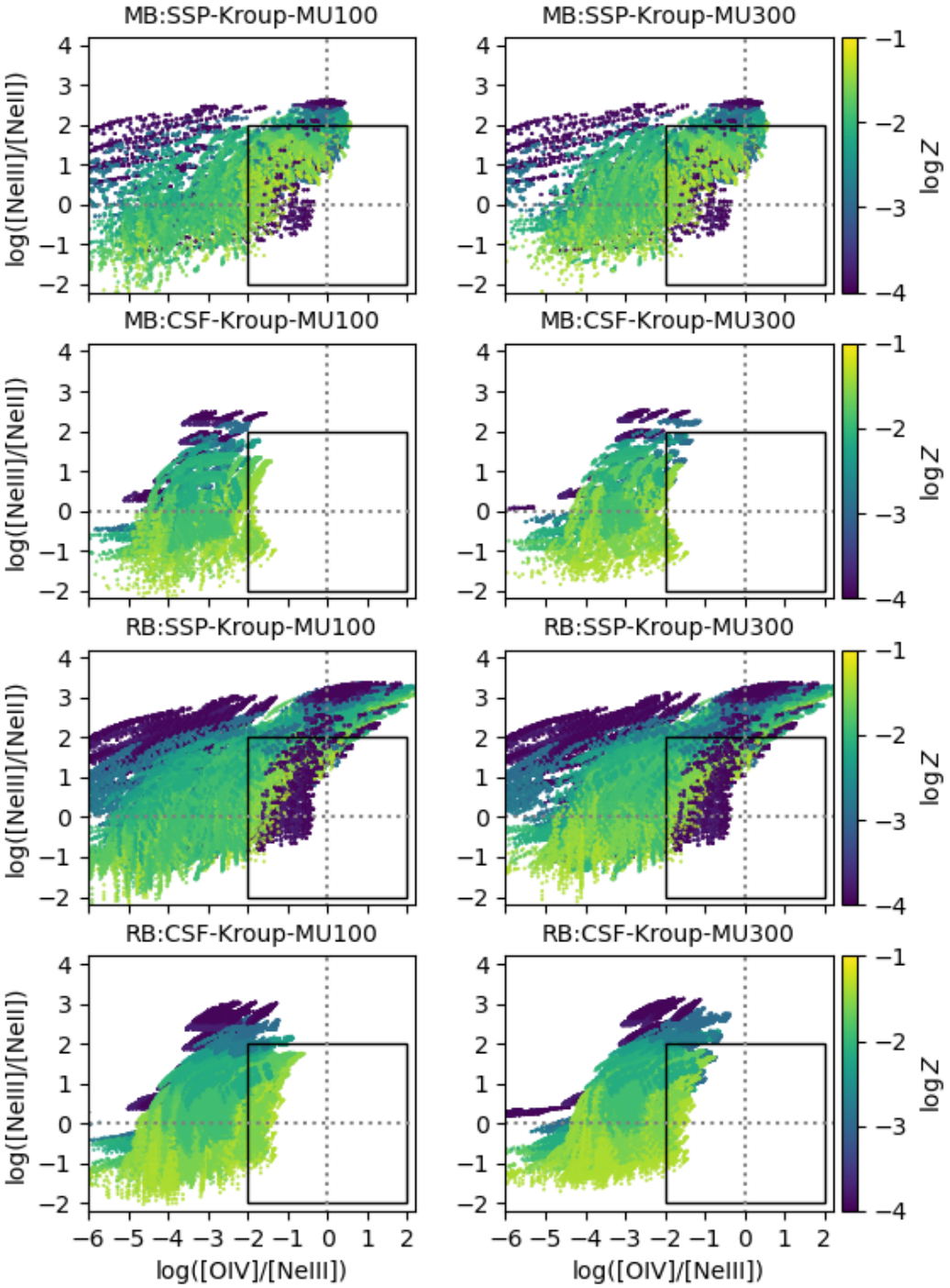

Figure 4. Synthetic log ([Ne III] λ15.6μm/[Ne II] λ12.8μm) vs. log ([O IV] λ25.9μm/[Ne III]) MIR diagnostic diagram from the SSP and CSF models assuming a Kroupa IMF with either $m_u = 100$ or 300 $M_\odot$. Models reaching the MB condition are shown in the *4-top panels*. The *4-bottom panels* show the RB models. Models are colour codded according to log Z as indicated in the colour-bar. We remark that the range of values of both line ratios plotted in these frames is considerably larger than the range of interest shown in Fig. 1, indicated by the inner square in each panel.

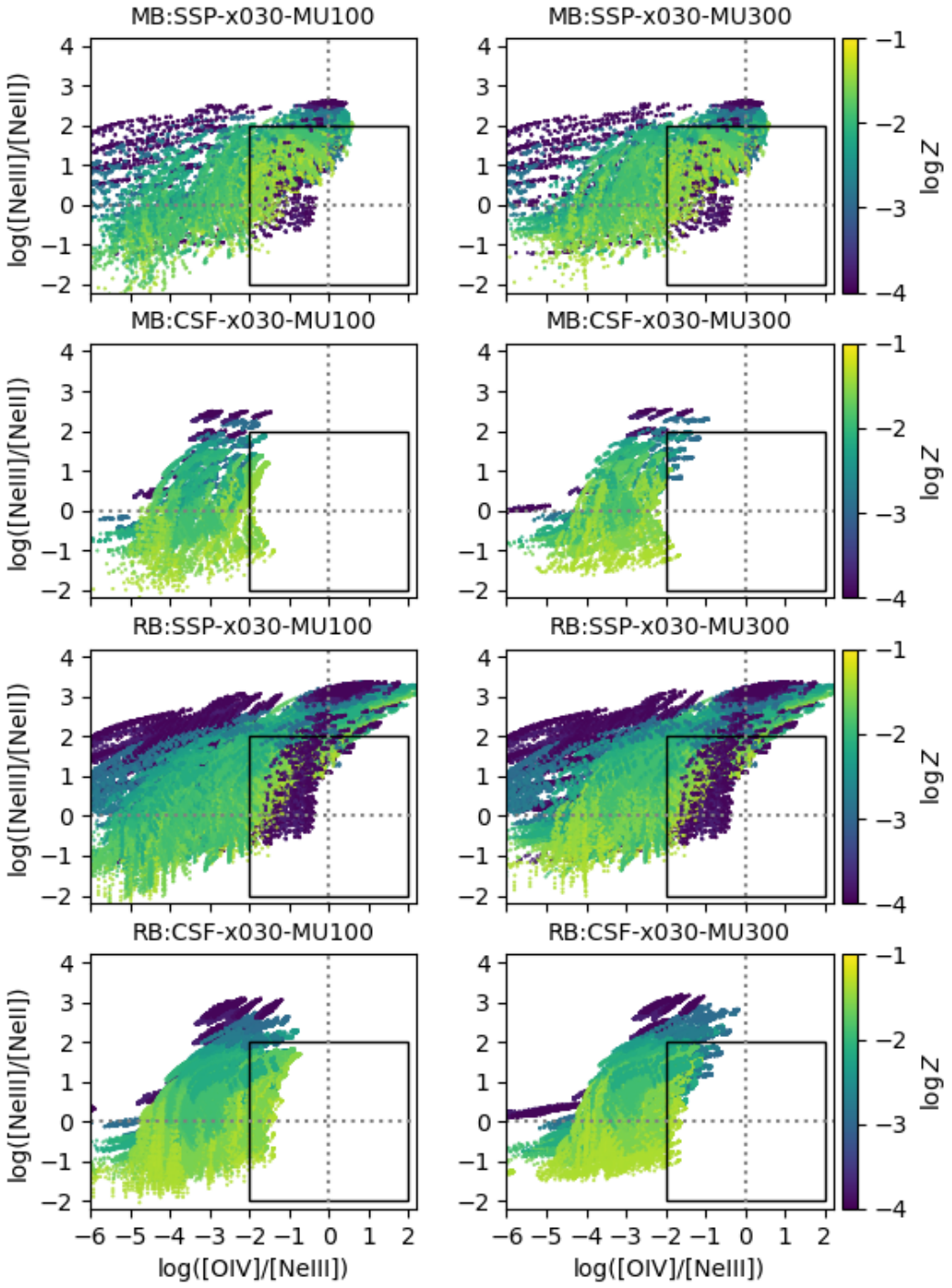

Figure 5. Same as Fig. 4 but for the x030 IMF.

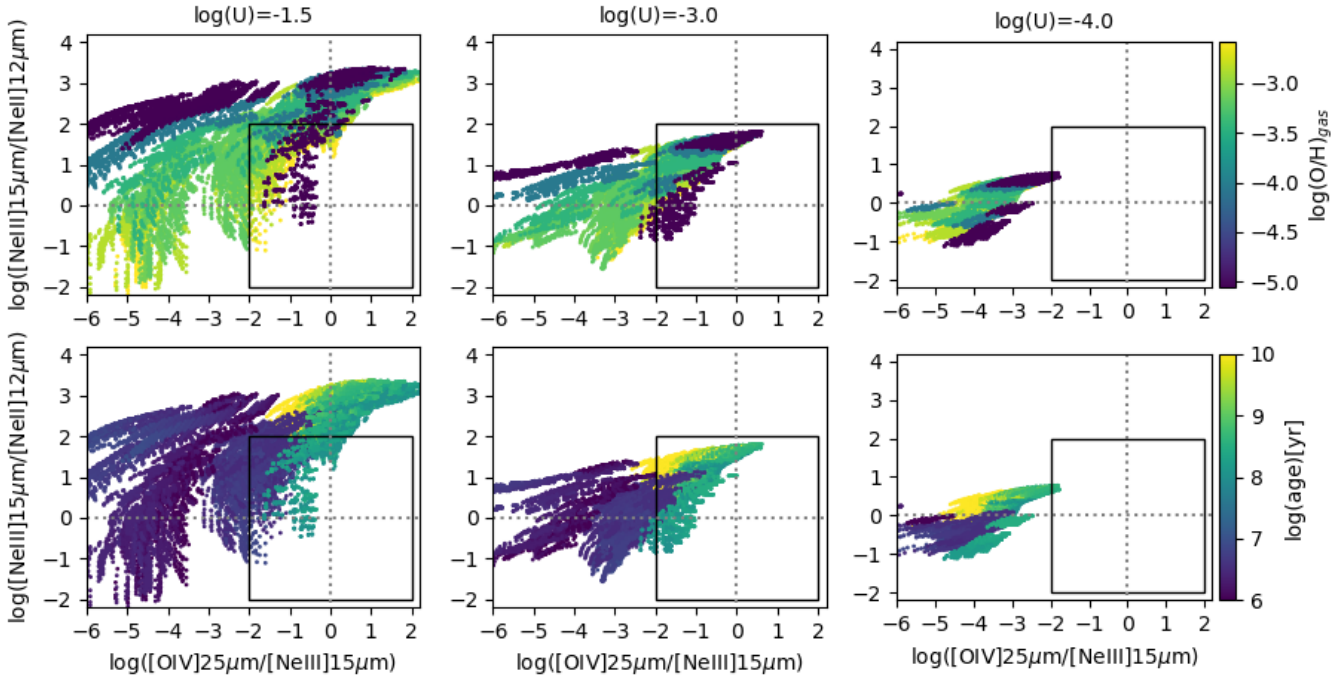

Figure 6. Synthetic log ([Ne III] λ15.6μm/[Ne II] λ12.8μm) vs. log ([O IV] λ25.9μm/[Ne III]) MIR diagnostic diagram for the RB-SSP-Kroup-MU100 models. *Left panels:* log (U) = -1.5. *Middle panels:* log (U) = -3. *Right panels:* log (U) = -4. Points are coded in size according to log n_e and colour coded according to log(O/H) (top panels) and age (bottom panels), as indicated by the colour bars.

5 BPT DIAGRAM

The classical BPT diagnostic diagram (Baldwin, Phillips & Terlevich 1981) is an important tool to discriminate between SF and AGN-dominated emission regions. However, since optical emission lines are affected by extinction, its classifying power decreases for low-luminosity and optically-obscured systems. In general, the optical spectra of SF galaxies (like WR and BCD galaxies) can be described by a population of Wolf-Rayet and massive hot OB stars, since they are the main source of UV radiation. However, in other galaxies, an additional ionising source, either UV radiation produced by a population of HOLMES or shocks, seems necessary to explain the observed emission line ratios (Feltre et al. 2023). In general, authors tend to use shock models to explain the excess of emission that cannot be reproduced by massive hot stars (e.g., Flores-Fajardo et al. 2011, and references therein). However, studying the optical and MIR colours of a sample of LINER-like galaxies, Flores-Fajardo et al. (2011) found that in these galaxies HOLMES are an important source of ionization.

In Fig. 11, we plot next to each other the MIR and BPT diagnostic diagrams for the RB-SSP-Kroup-MU100 photoionization models, colour-coded according to their position in the MIR diagram. Models (*green* dots) in quadrant III of the MIR diagram reach lower values of [O III]/Hβ than those in quadrants I and II (*blue* and *red* dots). However, most of these models have [O IV]/[Ne III] lower than -2. This may explain why there are so few *pure* SF galaxies in this zone with detected [O IV] λ25.9μm emission. The detection of [O IV] in galaxies that lie in this zone might indicate the presence of an additional source of excitation, like shocks driven by a weak AGN. On the other hand, a number of models in the HOLMES regime reach [O III]/Hβ ratios larger than in SB models. Using optical and MIR data for a LINER sample, Herpich et al. (2016) found that a non-negligible population of LINERs are retired galaxies, in which the star formation activity has stopped, giving pass to ionization powered by HOLMES.

Following Kewley et al. (2001) definition of a *maximum SB line*, we use the subset of our RB-SSP-Kroup-MU100 models with typical parameters log $(OH)_{gas}$ = -2.86, $\Delta N/O = 0$, C/O = -0.36, n_e = 10^2 cm^{-3}, age = 1 Gyr (e.g., Flores-Fajardo et al. 2011; Sokolowski & Bland-Hawthorn 1991), to define a new optical HOLMES *demarcation line* (HDL), described by the following fitted relation

$$\log([\mathrm{O\,III}]/\mathrm{H}\beta) < \frac{0.51}{\log([\mathrm{N\,II}]/\mathrm{H}\alpha) - 0.61} + 1.09, \quad (4)$$

representing the *maximum* contribution by HOLMES to the excitation in retired galaxies, avoiding the AGN-dominated region in the MIR diagnostic diagram. The HDL is plotted as a dashed line in the BPT diagram shown on the RHS panel of Fig. 11.

In Fig. 12 we plot models corresponding to extreme values in our grid of parameters, together with the HDL. These extreme models are among the *red* points in Fig. 11. In Fig. 12 models are shown at age = 1 Gyr for n_e in the range $10 - 10^4$ cm^{-3}. Models in the LHS panels, corresponding to (log $(OH)_{gas}$ = -2.86, $\Delta N/O = 0$, C/O = -0.36), with $n_e > 10^2$ cm^{-3}exceed the HDL limit and mimic the radiation field in AGN-dominated sources (Stasińska et al. 2015). Similarly, models in the middle (log $(OH)_{gas}$ = -2.58, $\Delta N/O$ = -0.25, C/O = -1), and RHS (log $(OH)_{gas}$ = -2.58, $\Delta N/O$ = 0.25, C/O = -1) panels exceed the HDL limit for all values of n_e. Most likely, these models overestimate the excitation because they are calculated assuming extreme values of $(OH)_{gas}$ and $\Delta N/O$ (see Fig. 1 in Gutkin,

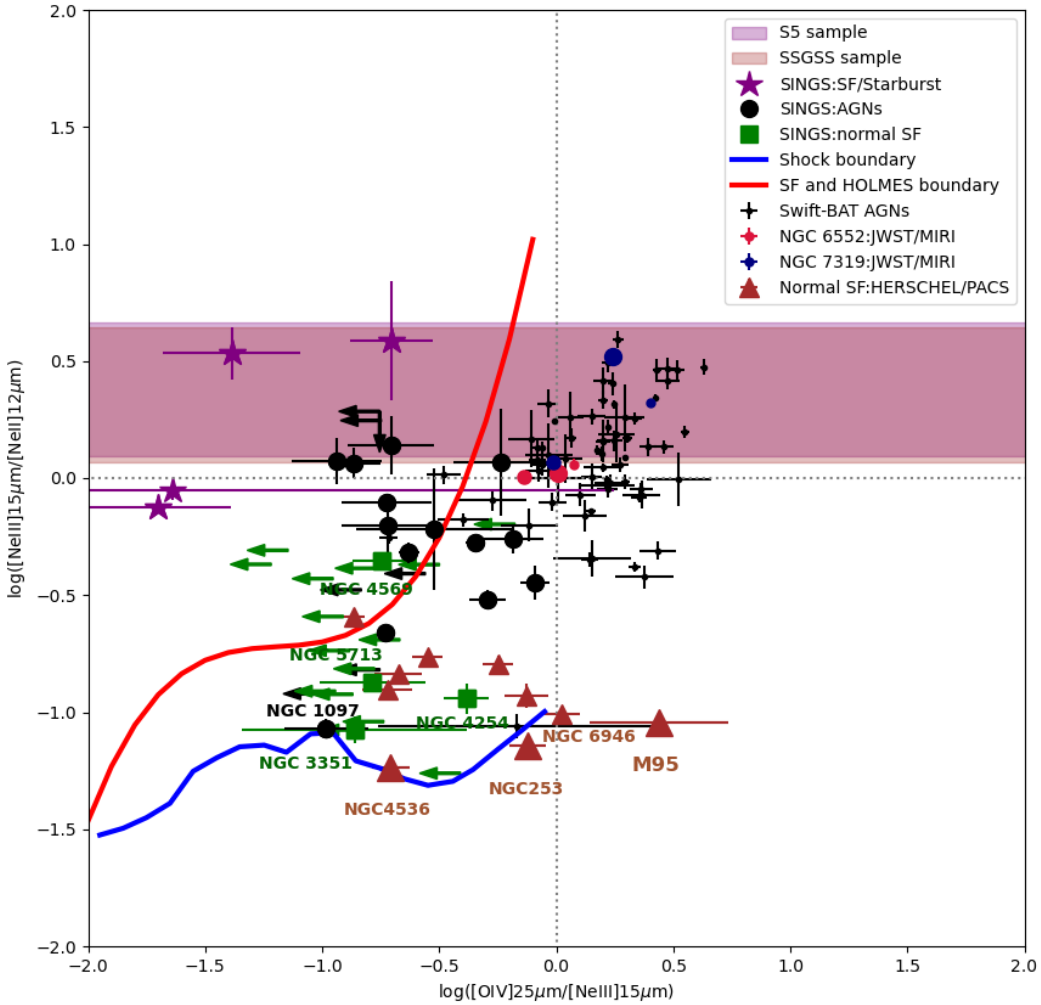

Figure 7. [Ne III] λ15.6μm/[Ne II] λ12.8μm vs. [O IV] λ25.9μm/[Ne III] λ15.6μm MIR diagnostic diagram. The *red* line represents the boundary of the SF-zone defined in Eq. (2). The *blue* line represents the lower-limit for the excitation from shock models in the normal-SF zone. The meaning of the various symbols is explained in the legend. The black and green arrows indicate upper limits. In the case of NGC 6552 the size of the *crimson* points corresponds to the nuclear (small), circumnuclear (medium), and central (large) emissions. In the case of NGC7319 the size of the *navy* points correspond to the nuclear (small), N2 (medium), S2 (large). Larger triangles are used to highlight individual objects.

Charlot, & Bruzual 2016). Therefore, the physical conditions of the models in the left panels of Fig. 12 with $n_H = 10^2$ cm^{-3} represent a more realistic scenario to model photoionization by HOLMES in retired galaxies.

In Fig. 13 we plot the HDL, Eq. (4), in the BPT diagram, together with AGN (*black*), SB (*purple*) and H II galaxy (*green*) observations. It is likely that AGNs that lie below the HDL are contaminated by emission due to HOLMES. Interestingly, whereas in the BPT diagram HII galaxies lie within the minimal AGN boundary (lines marked Ka03 and Me14 in Fig. 13; Kauffmann et al. 2003; Meléndez et al. 2014) and the maximum stellar boundaries (line marked Ke01; Kewley et al. 2001) and the HDL, in the mid-IR diagram most of them lie out of the star forming boundary, indicating that shocks, attributed to stellar feedback or/and AGN activity, are an important source of excitation. This result shows the robustness of using both the optical and IR diagnostic diagrams to classify deeply dust-enshrouded and obscured systems. A better comprehension of the ionising sources translates into a deeper understanding of the evolutionary path of these galaxies.

We remark that our SB models with $n_H = 10^2$ cm^{-3} are in agreement with the theoretical maximum SB line derived by Kewley et al. (2001) using the PEGASE v2.0 (Fioc & Rocca-Volmerange 1997) and Starburst99 (Leitherer et al. 1999) stellar population models and the MAPPINGS III (Sutherland & Dopita 1993) photoionization code, for $n_H = 10^2$ cm^{-3} and a maximum stellar age of 100 Myr. More complete studies with optical and IR samples of AGN and

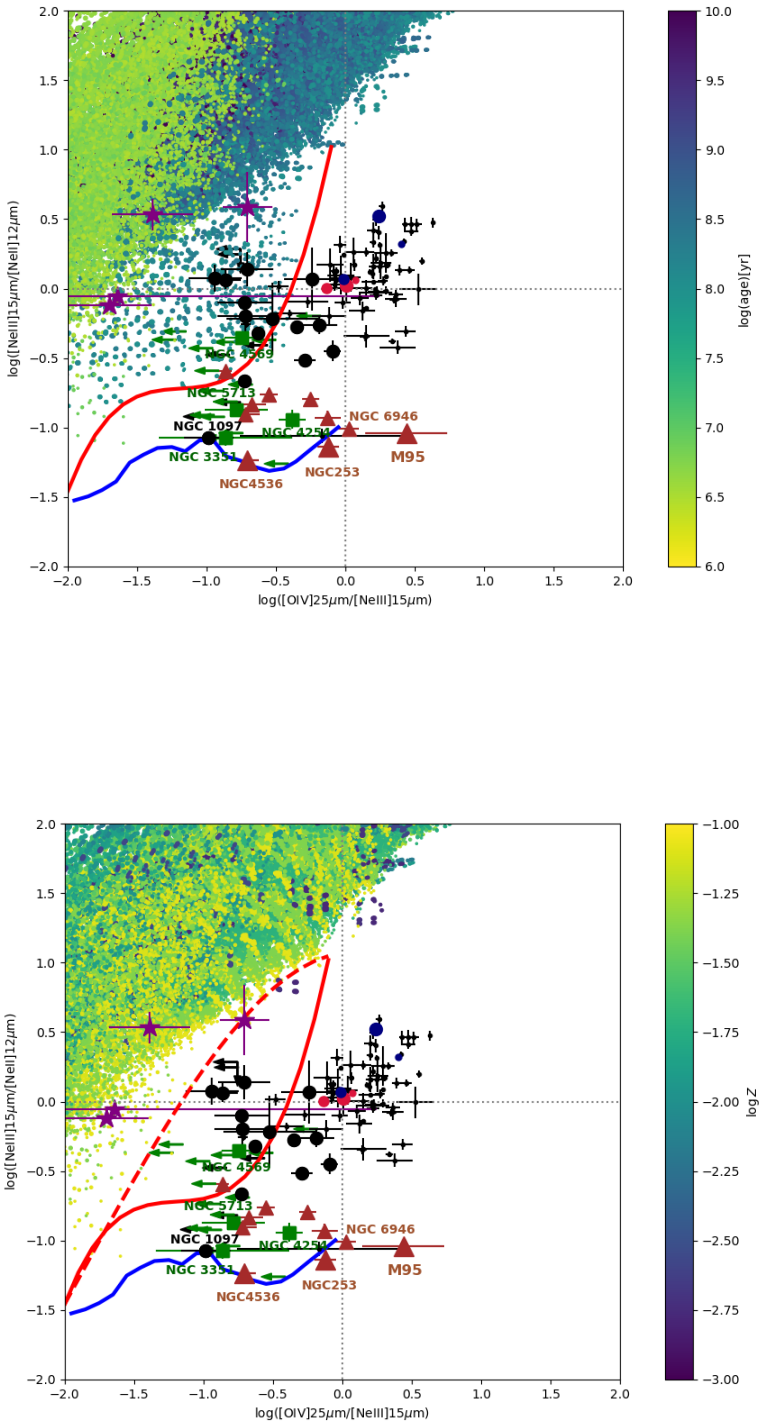

Figure 8. [Ne III] λ15.6μm/[Ne II] λ12.8μm vs. [O IV] λ25.9μm/[Ne III] λ15.6μm MIR diagnostic diagram. *Upper panel:* the *red solid* line represents the boundary of the SF-zone defined in Eq. (2). The models are colour coded by age according to the colour bar. *Bottom panel:* the *red dashed* line represents the boundary of the SF-zone defined in Eq. (3). The models are colour coded by metallicity according to the colour bar. In each panel the *blue* line represents the lower-limit for the excitation from shock models in the normal-SF zone. The meaning of the various symbols is explained in the legend in Fig. 7. The black and green arrows indicate upper limits. Larger triangles are used to highlight individual objects.

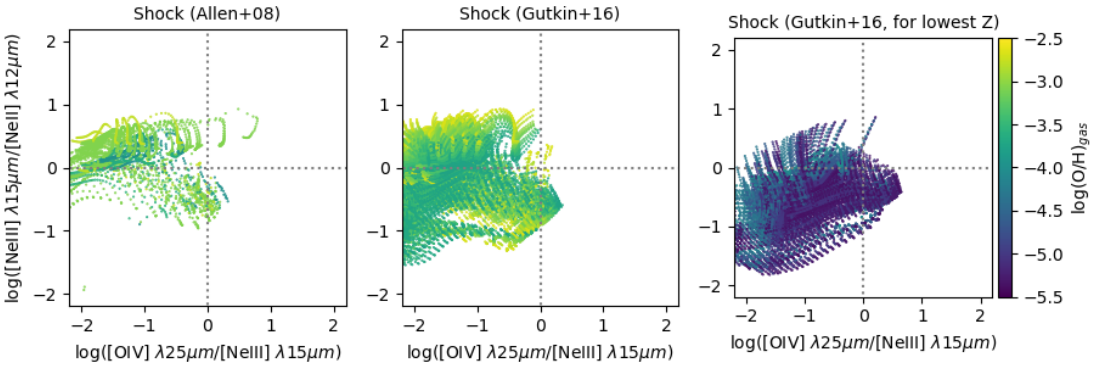

Figure 9. Position of shock models in the [Ne III] λ15.6μm/[Ne II] λ12.8μm vs. [O IV] λ25.9μm/[Ne III] λ15.6μm diagnostic diagram. *Left panel:* shock models computed by (Allen et al. 2008) using MAPPINGS V (Alarie & Morisset 2019). *Middle panel:* shock models computed by (Allen et al. 2008) using MAPPING V and assuming the abundances from (Gutkin, Charlot, & Bruzual 2016). *Right panel:* the same as in the *middle panel* but only for the lower metallicities. Note that we are plotting the Shock+Precursor models from (Alarie & Morisset 2019), available in the 3MdB database (Morisset et al. 2015). Points are colour coded according to log (O/H), as indicated in the colour bar.

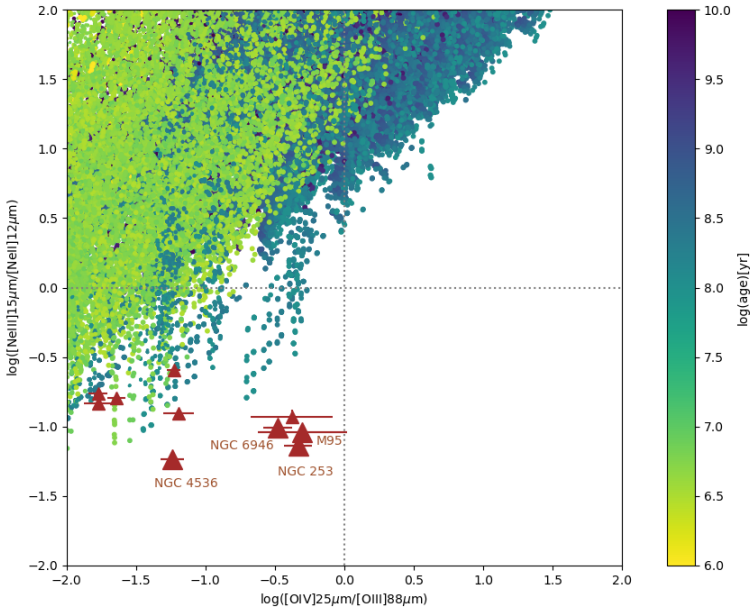

Figure 10. [Ne III] λ15.6μm/[Ne II] λ12.8μm vs. [O IV] λ25.9μm/[O III] λ88μm MIR-FIR diagnostic diagram proposed by Fernández-Ontiveros et al. (2016). The *triangles* show the Fernández-Ontiveros et al. (2016) *Herschel*/PACS observations listed in Table 2. Models are colour coded according to log age as indicated in the colour bar. Larger triangles are used to indicate individual objects.

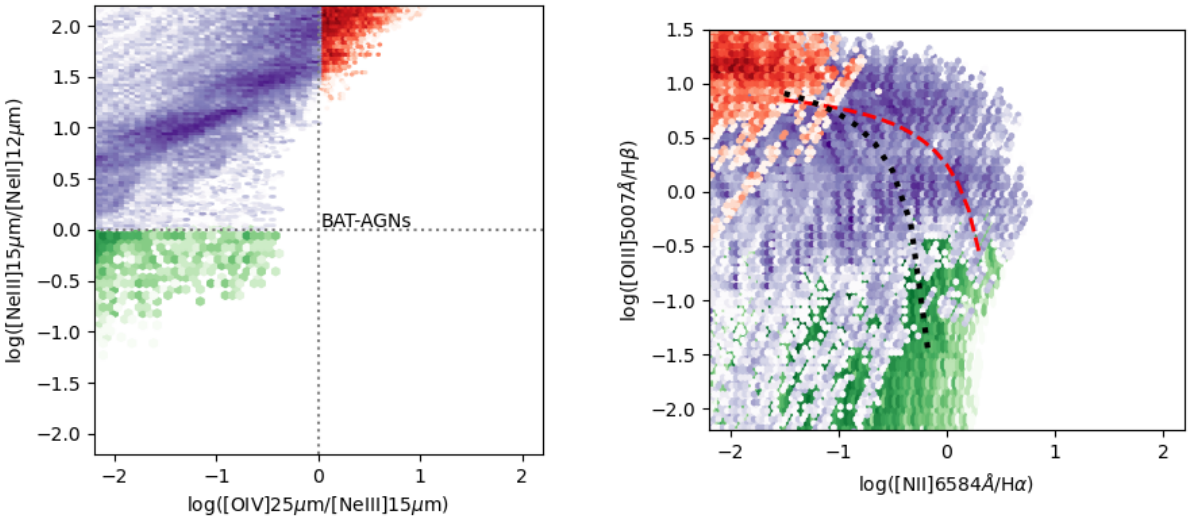

Figure 11. [Ne III] λ15.6μm/[Ne II] λ12.8μm vs. [O IV] λ25.9μm/[Ne III] λ15.6μm MIR diagnostic diagram (*left*) and BPT diagram (*right*). Models that in the MIR diagram lie in the quadrant III, quadrant II, and quadrant I are plotted in *green, blue* and *red*, respectively, in both diagrams. The HDL defined in Eq. (4) is plotted as a *red-dashed* line in the BPT diagram. The *black-dotted* line is the minimal AGN contribution from Kauffmann et al. (2003).

retired galaxies are needed to fully understand the different nature of their ionizing radiation.

6 SUMMARY AND CONCLUSIONS

In this paper we investigate the excitation mechanisms and the physical properties of the ionized gas of star forming galaxies appearing in the [Ne III]/[Ne II] vs. [O IV]/[Ne III] MIR diagnostic diagram proposed by Weaver et al. (2010). This MIR diagram is divided into four zones according to the value of the emission line ratios. Using the C&B stellar population models described in Plat et al. (2019) and Sánchez et al. (2022), together with the Cloudy photoionization code (Ferland et al. 2017), we calculate the intensity of the following optical, MIR and FIR emission lines: [O III] λ5007Å, Hβ, [N II] λ6583Å, Hα, [O IV] λ25.9μm, [Ne III] λ15.6μm, [Ne II] λ12.8μm and [O III] λ88μm, expected to be present in the spectra of SF galaxies.

We explore C&B models forming stars either in an instantaneous burst (SSP) of mass 1×10^6 M$_\odot$ or at a constant rate of 1 M$_\odot$ yr^{-1} (CSF). We compute these models for the Kroupa (Kroupa 2001) and a top-heavy ($x = 0.30$) IMF with two upper mass limits, $M_u = 100$ and 300 M$_\odot$. We assume seven stellar metallicities in the range $0.0002 < Z_* < 0.06$. To model both star forming and retired galaxies, we allow the age of the stellar population to vary from 1 Myr to 10 Gyr. For the photoionized clouds we vary the ionization parameter $\log(U)$, the hydrogen density n_H, and $\log(O/H)_{gas}$, $\Delta N/O$ and C/O as indicated in Table 4. The gas metal content is assumed to be the same as that of the ionising stars. We find that, in general, the MIR ([Ne III]/[Ne II] vs. [O IV]/[Ne III]) line ratios are insensitive to variations in the IMF slope and upper mass cut-off. Althought most models lie out of the range of interest (quadrant III in Fig. 1), a minor fraction falls in this quadrant. SSP models span a wider range of [Ne III]/[Ne II] vs. [O IV]/[Ne III] line ratios. Therefore, for simplicity, we base our analysis on radiation bounded (RB) models with $M_u = 100$ M$_\odot$ and Kroupa IMF (named RB-SSP-Kroup-MU100 models). These models fall both in quadrants II (WR Galaxies/BCD Galaxies) and III (SB Galaxies/HII Galaxies).

To constrain our models we compare our results with the optical, MIR and FIR observations available for a few H II galaxies, SB and AGN (Table 2), and the optical emission lines of the BAT-AGN sample. We also compare our predictions with spatially resolved *JWST*/MIRI observations of two nearby AGNs.

We derive the lower boundary limiting models with stellar age from 100 to 1000 Myr and $0.0002 < Z_* < 0.06$. We find that low metallicity models lie close to the boundary in quadrants II and III. In particular, most models in quadrant III have the lowest Z_* ($\log Z_* < -3$). We derive a second lower boundary by ignoring the lower Z_* models, which clearly excludes the weak AGNs from the SINGS sample, as well as all the H II galaxies. We conclude that excitation by AGN-driven shocks is most likely the dominant ionising source in some galaxies in quadrant III. We highlight that both the MIR diagnostic diagram and the spatially resolved *JWST*/MIRI data are powerful tools to disentangle the different sources of ionization, especially in galaxies with a complex evolutionary dynamic, in which AGNs, shocks, and a mixture of stellar populations may coexist.

In particular, our models reproduce the observed MIR line ratios of NGC 4569 (Fig. 8), one of the four H II galaxies in the SINGS sample in Table 2, suggesting that mainly low metallicity HOLMES are responsible for the ionization in this galaxy. In Fig. 8, NGC 5713 and NGC 4254 are in agreement with shock models, whereas NGC 3351 lies below the SF boundary and close to the shock boundary. The emission of [O IV] λ25.9μm in NGC 3351 could point to the presence of a weak AGN, as in the case of NGC 4536 and NGC 253, which show evidence of a weak AGN and have similar MIR emission line

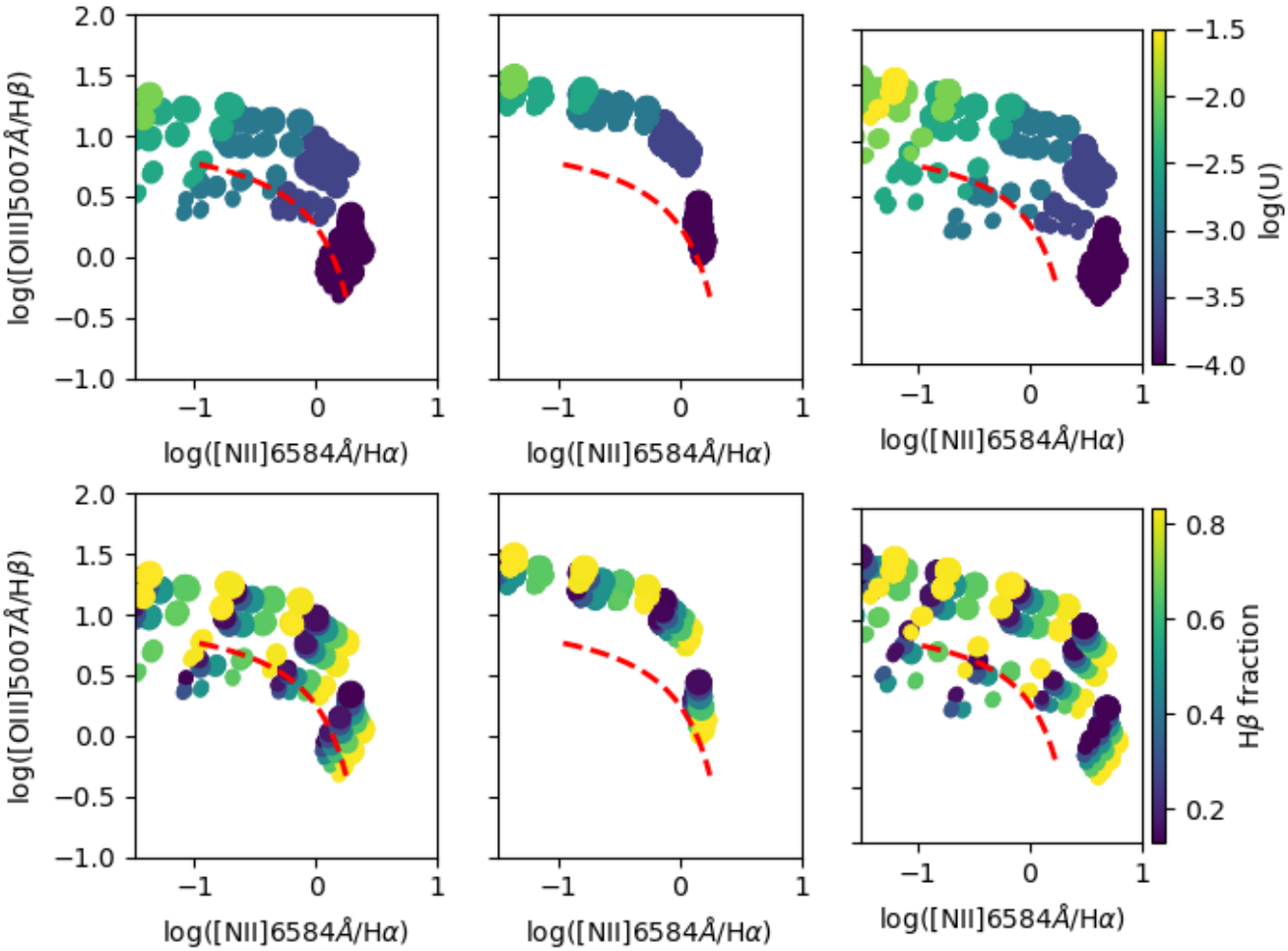

Figure 12. Position of the RB-SSP-Kroup-MU100 models with extreme values of parameters in the BPT diagram. Models are shown at age = 1 Gyr for $\Delta N/O = 0$, C/O = -0.36 (*left*), $\Delta N/O$ = -0.25, C/O = -1 (*middle*) and $\Delta N/O$ = +0.25, C/O = -1 (*right*). In the upper panels the points are colour coded according to log (U), as indicated in the color bar. In the bottom panels the points are colour coded according to H_β fraction. In each panel the size of the points increases with n_e and the HDL, defined by Eq. (4), is plotted as a *red-dashed* line.

ratios to NGC 3351. Only five of the ten H II galaxies with MIR and FIR observations are reproduced by this set of SSP models (Fig. 10). For the remaining objects, the high emission of [O IV] λ25.9μm can be attributed again to the presence of a weak AGN.

From the boundary traced in the BPT diagram by our Kroupa IMF (M_u = 100 $M_\odot$) SSP models (Fig. 11), we derive a new optical demarcation line, which represents the maximum contribution to line emission by massive stars in SB and HOLMES in retired galaxies, without invading the AGN-dominated region. This line predicts a larger contribution to the emission due to the inclusion of the HOLMES far-UV continuum. If this far-UV emission is excluded, our models reproduce the classical demarcation line previously derived by Kewley et al. (2001).

Considering that the far-UV ionising radiation from HOLMES results in emission line ratios that mimic those in AGN, a non-negligible population of (weak) AGNs may be misclassified. Detailed observational studies about the role of this population in the optical and MIR spectral ranges need to be done. MIR spectra from *JWST*/MIRI will allow detailed studies of [O IV] λ25.9μm emission in local AGN, SB, and H II galaxies.

7 DATA AVAILABILITY

The data underlying this article are available in [the Mexican Million Model database] at [https://sites.google.com/site/mexicanmillionmodels/the-different-projects/cb_19?pli=1], and can be accessed with the reference code [CB_19].

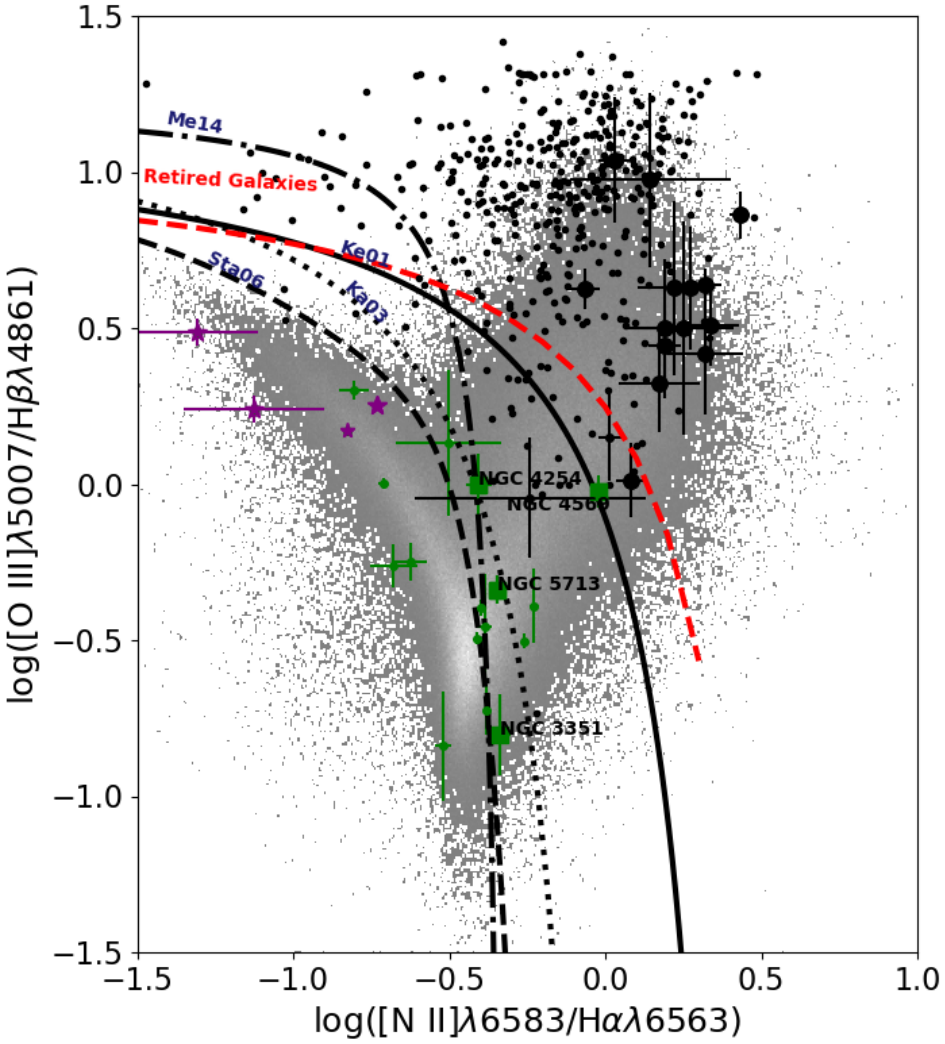

Figure 13. Position of various demarcation lines in the BPT diagram. The *red-dashed* line represents the HDL defined in Eq. (4). The *black-dot-dashed* line represents the minimum AGN contribution derived by Meléndez et al. (2014, Me14). The *black-dashed* line is the theoretical limit for the pure SF galaxies from Stasińska et al. (2006, Sta06). The *black-solid* line is the theoretical maximum contribution from SB calculated by Kewley et al. (2001, Ke01). The *black-dotted* line is the minimal AGN contribution from Kauffmann et al. (2003, Ka03). The meaning of the *purple, green* and *large-black* symbols is the same as in Fig. 7. The *small-black* points are from the BAT-AGN sample (Koss et al. 2017). The *grey-dots* are galaxies from the SDSS DR8 selected with signal-to-noise ratio > 3 σ (see Brinchmann et al. 2004; Tremonti et al. 2004).

ACKNOWLEDGEMENTS

Calculations were performed with version 17.03 of Cloudy, described by Ferland et al. (2017). This work is based partially on observations made with the NASA/ESA/CSA James Webb Space Telescope. The data were obtained from the Mikulski Archive for Space Telescopes at the Space Telescope Science Institute, which is operated by the Association of Universities for Research in Astronomy, Inc., under NASA contract NAS 5-03127 for JWST. These observations are associated with programs No. 1039 and 2732. We thank S. Charlot for useful discussions. GB acknowledges financial support from the National Autonomous University of México (UNAM) through grants DGAPA/PAPIIT IG100319 and BG100622. CM acknowledges the support from UNAM/DGAPA/PAPIIT grant IN101220. MK acknowledges the support from the Korea Astronomy and Space Science Institute under the R&D program(Project No. 2022184009) supervised by the Ministry of Science and ICT.

REFERENCES

Alarie A., Morisset C., 2019, RMxAA, 55, 377. doi:10.22201/ia.01851101p.2019.55.02.21

Allen M. G., Groves B. A., Dopita M. A., Sutherland R. S., Kewley L. J., 2008, ApJS, 178, 20. doi:10.1086/589652

Álvarez-Márquez J., Labiano A., Guillard P., Dicken D., Argyriou I., Patapis P., Law D. R., et al., 2022, arXiv, arXiv:2209.01695
Aoki K., Kosugi G., Wilson A. S., Yoshida M., 1999, ApJ, 521, 565. doi:10.1086/307559
Armus L. et al., 2007, ApJ, 656, 148
Baldwin J. A., Phillips M. M., Terlevich R., 1981, PASP, 93, 5
Barth A. J., Shields J. C., 2000, PASP, 112, 753. doi:10.1086/316583
Beck A., Lebouteiller V., Madden S. C., Iserlohe C., Krabbe A., Ramambason L., Fischer C., et al., 2022, A&A, 665, A85. doi:10.1051/0004-6361/202243822
Bernard-Salas J. et al., 2009, ApJS, 184, 230
Binette L., Magris C. G., Stasińska G., Bruzual A. G., 1994, A&A, 292, 13
Boselli A., Boissier S., Cortese L., Gil de Paz A., Seibert M., Madore B. F., Buat V., et al., 2006, ApJ, 651, 811. doi:10.1086/507766
Brandl B. R. et al., 2006, ApJ, 653, 1129
Bressan A., Marigo P., Girardi L., Salasnich B., Dal Cero C., Rubele S., Nanni A., 2012, MNRAS, 427, 127
Brinchmann J., Charlot S., White S. D. M., Tremonti C., Kauffmann G., Heckman T., Brinkmann J., 2004, MNRAS, 351, 1151. doi:10.1111/j.1365-2966.2004.07881.x
Brookes M. H., Best P. N., Rengelink R., Röttgering H. J. A., 2006, MNRAS, 366, 1265. doi:10.1111/j.1365-2966.2005.09916.x
Bruzual G., Charlot S., 2003, MNRAS, 344, 1000
Calzetti D., Battisti A. J., Shivaei I., Messa M., Cignoni M., Adamo A., Dale D. A., et al., 2021, ApJ, 913, 37. doi:10.3847/1538-4357/abf118
Cazzoli S., Hermosa Muñoz L., Márquez I., Masegosa J., Castillo-Morales Á., Gil de Paz A., Hernández-García L., et al., 2022, A&A, 664, A135. doi:10.1051/0004-6361/202142695
Chen Y., Bressan A., Girardi L., Marigo P., Kong X., Lanza A., 2015, MNRAS, 452, 1068
Clark P. C., Glover S. C. O., 2014, MNRAS, 444, 2396. doi:10.1093/mnras/stu1589
Dale D. A. et al., 2006, ApJ, 646, 161
Dale D. A., Smith J. D. T., Schlawin E. A., Armus L., Buckalew B. A., Cohen S. A., Helou G. et al., 2009, ApJ, 693, 1821. doi:10.1088/0004-637X/693/2/1821
Dudik R. P., Weingartner J. C., Satyapal S., Fischer J., Dudley C. C., O'Halloran B., 2007, ApJ, 664, 71
Esquej P., Alonso-Herrero A., González-Martín O., Hönig S. F., Hernán-Caballero A., Roche P., Ramos Almeida C. et al., 2014, ApJ, 780, 86. doi:10.1088/0004-637X/780/1/86
Eskridge P. B., Frogel J. A., Pogge R. W., Quillen A. C., Berlind A. A., Davies R. L., DePoy D. L., et al., 2002, ApJS, 143, 73. doi:10.1086/342340
Farrah D. et al., 2007, ApJ, 667, 149
Ferland G. J. et al., 2017, RMxAA, 53, 385
Feltre A., Gruppioni C., Marchetti L., Mahoro A., Salvestrini F., Mignoli M., Bisigello L., et al., 2023, arXiv, arXiv:2301.02252. doi:10.48550/arXiv.2301.02252
Fernández-Ontiveros J. A., Spinoglio L., Pereira-Santaella M., Malkan M. A., Andreani P., Dasyra K. M., 2016, ApJS, 226, 19
Fioc M., Rocca-Volmerange B., 1997, A&A, 500, 507
Flores-Fajardo N., Morisset C., Stasińska G., Binette L., 2011, MNRAS, 415, 2182. doi:10.1111/j.1365-2966.2011.18848.x
García-Bernete I., González-Martín O., Ramos Almeida C., Alonso-Herrero A., Martínez-Paredes M., Ward M. J., Roche P. F., et al., 2022, A&A, 667, A140. doi:10.1051/0004-6361/202244230
García-Hernández D. A., Perea-Calderón J. V., Bobrowsky M., García-Lario P., 2006, IAUS, 234, 397. doi:10.1017/S1743921306003425
Genzel R. et al., 1998, ApJ, 498, 579
Girardi L., Bressan A., Bertelli G., Chiosi C., 2000, A&AS, 141, 371. doi:10.1051/aas:2000126
Goulding A. D., Alexander D. M., 2009, MNRAS, 398, 1165
Groves B. A., Dopita M. A., Sutherland R. S., 2004, ApJS, 153, 75. doi:10.1086/421114
Gutkin J., Charlot S., Bruzual G., 2016, MNRAS, 462, 1757. doi:10.1093/mnras/stw1716
Hamann W.-R., Gräfener G., 2004, A&A, 427, 697
Hao L. et al., 2009, ApJ, 704, 1159
Herpich F., Mateus A., Stasińska G., Cid Fernandes R., Vale Asari N., 2016, MNRAS, 462, 1826. doi:10.1093/mnras/stw1742
Ho L. C., Filippenko A. V., Sargent W. L. W., 1997, ApJ, 487, 591. doi:10.1086/304643
Ho L. C., Filippenko A. V., Sargent W. L. W., 1997, ApJ, 487, 579. doi:10.1086/304642
Ho L. C., Keto E., 2007, ApJ, 658, 314. doi:10.1086/511260
Hughes M. A., Axon D., Atkinson J., Alonso-Herrero A., Scarlata C., Marconi A., Batcheldor D. et al., 2005, AJ, 130, 73. doi:10.1086/430531
Hunter D. A., Kaufman M., 2007, AJ, 134, 721
Jensen J. J. et al., 2017, MNRAS, 470, 3071
Kaplan K. F., Jogee S., Kewley L., Blanc G. A., Weinzirl T., Song M., Drory N., et al., 2016, MNRAS, 462, 1642. doi:10.1093/mnras/stw1422
Kauffmann G., Heckman T. M., Tremonti C., Brinchmann J., Charlot S., White S. D. M., Ridgway S. E. et al., 2003, MNRAS, 346, 1055. doi:10.1111/j.1365-2966.2003.07154.x
Kennicutt R. C., Keel W. C., Blaha C. A., 1989, AJ, 97, 1022. doi:10.1086/115046
Kewley L. J., Dopita M. A., Sutherland R. S., Heisler C. A., Trevena J., 2001, ApJ, 556, 121. doi:10.1086/321545
Kewley L. J., Heisler C. A., Dopita M. A., Lumsden S., 2001, ApJS, 132, 37. doi:10.1086/318944
Kewley L. J., Groves B., Kauffmann G., Heckman T., 2006, MNRAS, 372, 961. doi:10.1111/j.1365-2966.2006.10859.x
Keel W. C., 1996, PASP, 108, 917. doi:10.1086/133813
Koss M., Trakhtenbrot B., Ricci C., Lamperti I., Oh K., Berney S., Schawinski K. et al., 2017, ApJ, 850, 74. doi:10.3847/1538-4357/aa8ec9
Kroupa P., 2001, MNRAS, 322, 231
LaMassa S. M., Heckman T. M., Ptak A., Schiminovich D., O'Dowd M., Bertincourt B., 2012, ApJ, 758, 1. doi:10.1088/0004-637X/758/1/1
Lanz T., Hubeny I., 2003, ApJS, 146, 417
Lanz T., Hubeny I., 2007, ApJS, 169, 83
Leitherer C. et al., 1999, ApJS, 123, 3
Levesque E. M., Kewley L. J., Berger E., Zahid H. J., 2010, AJ, 140, 1557. doi:10.1088/0004-6256/140/5/1557
Lutz D., Kunze D., Spoon H. W. W., Thornley M. D., 1998, A&A, 333, L75
Martínez-Paredes M., Aretxaga I., González-Martín O., Alonso-Herrero A., Levenson N. A., Ramos Almeida C., López-Rodríguez E., 2019, ApJ, 871, 190. doi:10.3847/1538-4357/aafa18
Martínez-Paredes M., González-Martín O., Esparza-Arredondo D., Kim M., Alonso-Herrero A., Krongold Y., Hoang T., et al., 2020, ApJ, 890, 152. doi:10.3847/1538-4357/ab6732
Martini P., Regan M. W., Mulchaey J. S., Pogge R. W., 2003, ApJS, 146, 353. doi:10.1086/367817
Mazzitelli I., D'Antona F., Ventura P., 1999, A&A, 348, 846
Meléndez M. et al., 2008, ApJ, 682, 94
Meléndez M., Heckman T. M., Martínez-Paredes M., Kraemer S. B., Mendoza C., 2014, MNRAS, 443, 1358
Miller Bertolami M. M., 2016, A&A, 588, A25. doi:10.1051/0004-6361/201526577
Mello D. R. C., Daflon S., Pereira C. B., Hubeny I., 2012, A&A, 543, A11. doi:10.1051/0004-6361/201117591
Mohan N. R., Anantharamaiah K. R., Goss W. M., 2002, ApJ, 574, 701. doi:10.1086/341004
Morisset, C., Delgado-Inglada, G., & Flores-Fajardo, N., 2015, RMAA, 51, 103-120
Moumen I., Robert C., Devost D., Martin R. P., Rousseau-Nepton L., Drissen L., Martin T., 2019, MNRAS, 488, 803. doi:10.1093/mnras/stz1734
Moustakas J., Kennicutt R. C., Tremonti C. A., Dale D. A., Smith J.-D. T., Calzetti D., 2010, ApJS, 190, 233. doi:10.1088/0067-0049/190/2/233
Nicholls D. C., Sutherland R. S., Dopita M. A., Kewley L. J., Groves B. A., 2017, MNRAS, 466, 4403. doi:10.1093/mnras/stw3235
Plat A., Charlot S., Bruzual G., Feltre A., Vidal-García A., Morisset C., Chevallard J., et al., 2019, MNRAS, 490, 978. doi:10.1093/mnras/stz2616
Peeters E., Spoon H. W. W., Tielens A. G. G. M., 2004, ApJ, 613, 986
Pereira-Santaella M., Diamond-Stanic A. M., Alonso-Herrero A., Rieke G. H., 2010, ApJ, 725, 2270

Pereira-Santaella M., Álvarez-Márquez J., García-Bernete I., Labiano A., Colina L., Alonso-Herrero A., Bellocchi E., et al., 2022, A&A, 665, L11. doi:10.1051/0004-6361/202244725
Ptak A., Serlemitsos P., Yaqoob T., Mushotzky R., Tsuru T., 1997, AJ, 113, 1286. doi:10.1086/118342
Pontoppidan K. M., Barrientes J., Blome C., Braun H., Brown M., Carruthers M., Coe D., et al., 2022, ApJL, 936, L14. doi:10.3847/2041-8213/ac8a4e
Rauch T., 2002, RMxAC, 12, 150, RMxAC..12
Rauch T., 2003, A&A, 403, 709. doi:10.1051/0004-6361:20030412
Rhea C. L., Rousseau-Nepton L., Moumen I., Prunet S., Hlavacek-Larrondo J., Grasha K., Robert C., et al., 2023, RASTI, 2, 345. doi:10.1093/rasti/rzad023
Richardson C. T., Allen J. T., Baldwin J. A., Hewett P. C., Ferland G. J., Crider A., Meskhidze H., 2016, MNRAS, 458, 988. doi:10.1093/mnras/stw100
Rodríguez-Merino L. H., Chavez M., Bertone E., Buzzoni A., 2005, ApJ, 626, 411
Salpeter E. E., 1955, ApJ, 121, 161
Sánchez S. F., Barrera-Ballesteros J. K., Lacerda E., Mejía-Narvaez A., Camps-Fariña A., Bruzual G., Espinosa-Ponce C., et al., 2022, ApJS, 262, 36. doi:10.3847/1538-4365/ac7b8f
Satyapal S., Vega D., Dudik R. P., Abel N. P., Heckman T., 2008, ApJ, 677, 926
Sérsic J. L., 1973, PASP, 85, 103. doi:10.1086/129413
Smith J. D. T., Draine B. T., Dale D. A., Moustakas J., Kennicutt R. C., Helou G., Armus L. et al., 2007, ApJ, 656, 770. doi:10.1086/510549
Sokolowski J., Bland-Hawthorn J., 1991, PASP, 103, 911. doi:10.1086/132906
Spinoglio L., Pereira-Santaella M., Dasyra K. M., Calzoletti L., Malkan M. A., Tommasin S., Busquet G., 2015, ApJ, 799, 21. doi:10.1088/0004-637X/799/1/21
Spoon H. W. W. et al., 2007, ApJL, 654, L49
Stasińska G., Cid Fernandes R., Mateus A., Sodré L., Asari N. V., 2006, MNRAS, 371, 972. doi:10.1111/j.1365-2966.2006.10732.x
Stasińska G., Vale Asari N., Cid Fernandes R., Gomes J. M., Schlickmann M., Mateus A., Schoenell W. et al., 2008, MNRAS, 391, L29. doi:10.1111/j.1745-3933.2008.00550.x
Stasińska G., Costa-Duarte M. V., Vale Asari N., Cid Fernandes R., Sodré L., 2015, MNRAS, 449, 559. doi:10.1093/mnras/stv078
Stasińska, G., Izotov, Y., Morisset, C., and Guseva, N. , 2015, A&A, 576, A83
Stasińska G., Trevisan M., Vale Asari N., 2022, FrASS, 9, 913485. doi:10.3389/fspas.2022.913485
Sturm E. et al., 2002, A&A, 393, 821
Sturm E. et al., 2006, ApJL, 653, L13
Sutherland R. S., Dopita M. A., 1993, ApJS, 88, 253. doi:10.1086/191823
Sutherland R. S., Dopita M. A., 2017, ApJS, 229, 34. doi:10.3847/1538-4365/aa6541
Schweitzer M., Lutz D., Sturm E., Contursi A., Tacconi L. J., Lehnert M. D., Dasyra K. M. et al., 2006, ApJ, 649, 79. doi:10.1086/506510
Tremonti C. A., Heckman T. M., Kauffmann G., Brinchmann J., Charlot S., White S. D. M., Seibert M. et al., 2004, ApJ, 613, 898. doi:10.1086/423264
van Winckel H., 2003, ARA&A, 41, 391. doi:10.1146/annurev.astro.41.071601.170018
Vassiliadis E., Wood P. R., 1993, ApJ, 413, 641. doi:10.1086/173033
Veilleux S., Osterbrock D. E., 1987, NASCP, 737, NASCP2466
Weaver K. A. et al., 2010, ApJ, 716, 1151
Webster B. L., Smith M. G., 1983, MNRAS, 204, 743. doi:10.1093/mnras/204.3.743
Weedman D. et al., 2006, ApJ, 653, 101
Zhang X., Feng Y., Chen H., Yuan Q., 2020, ApJ, 905, 97. doi:10.3847/1538-4357/abc478

APPENDIX A: BPT DIAGRAMS

In Figs. A1 and A2 we show, respectively, the BPT diagrams for the Kroupa and X030 IMF SSP and CSF models, for both $m_u = 100$ and 300 $M_\odot$. Models reaching the MB condition are shown in the *top panels*. The *bottom panels* show the RB models.

This paper has been typeset from a TEX/LATEX file prepared by the author.

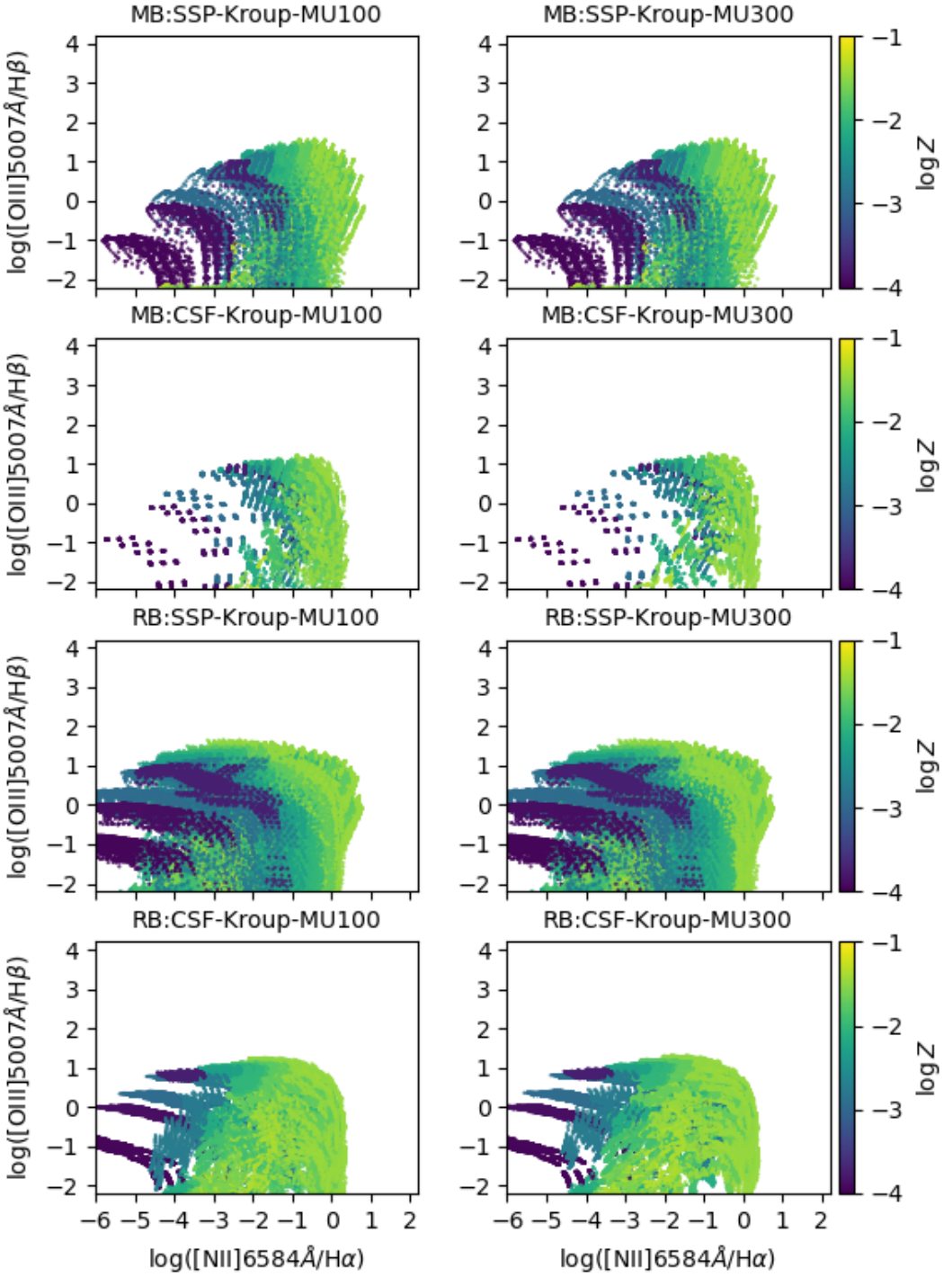

Figure A1. Same as Fig. 4 but for the optical ratios.

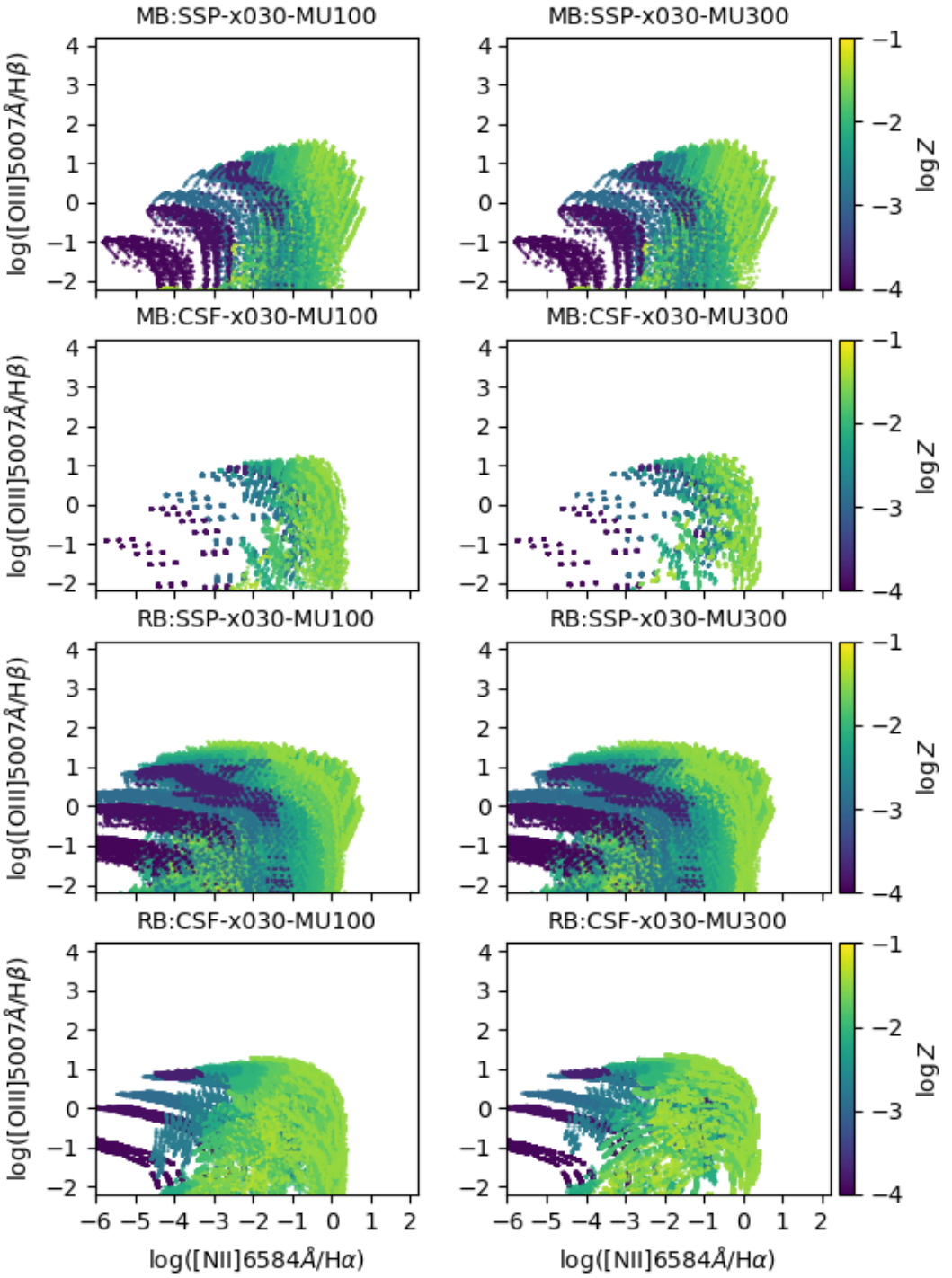

Figure A2. Same as Fig. 5 but for the optical ratios.